

A Review of NEST Models, and Their Application to Improvement of Particle Identification in Liquid Xenon Experiments

M. Szydagis,^{1,*} J. Balajthy,^{2,3} G.A. Block,^{1,4} J.P. Brodsky,⁵ E. Brown,⁴ J.E. Cutter,^{2,6} S.J. Farrell,⁷ J. Huang,^{2,8} A.C. Kamaha,⁹ E.S. Kozlova,^{10,11} C.S. Liebenthal,⁷ D.N. McKinsey,^{12,13} K. McMichael,⁴ M. Mooney,¹⁴ J. Mueller,¹⁴ K. Ni,⁸ G.R.C. Rischbieter,¹ M. Tripathi,² C.D. Tunnell,⁷ V. Velan,^{12,13} M.D. Wyman,¹ Z. Zhao,⁸ and M. Zhong⁸

¹*Department of Physics, University at Albany, State University of New York,
1400 Washington Ave., Albany, NY 12222, USA*

²*Department of Physics, University of California Davis, One Shields Ave., Davis, CA 95616, USA*

³*Sandia National Laboratories, Livermore, CA 94550, USA*

⁴*Department of Physics, Applied Physics and Astronomy,
Rensselaer Polytechnic Institute, Troy, NY 12180, USA*

⁵*Lawrence Livermore National Laboratory, 7000 East Ave., Livermore, CA 94551, USA*

⁶*Deepgram, Mountain View, CA 94103, USA*

⁷*Department of Physics and Astronomy, Rice University, Houston, TX 77005, USA*

⁸*Department of Physics, University of California San Diego, La Jolla, CA 92093, USA*

⁹*Department of Physics and Astronomy, University of California Los Angeles, Los Angeles, CA 90095-1547, USA*

¹⁰*Institute for Theoretical and Experimental Physics Named by A.I. Alikhanov
of National Research Centre “Kurchatov Institute,” 117218 Moscow, Russia*

¹¹*Moscow Engineering Physics Institute (MEPhI),
National Research Nuclear University 115409 Moscow, Russia*

¹²*Lawrence Berkeley National Laboratory, 1 Cyclotron Rd., Berkeley, CA 94720, USA*

¹³*Department of Physics, University of California Berkeley, Berkeley, CA 94720, USA*

¹⁴*Department of Physics, Colorado State University, Fort Collins, CO 80523, USA*

This paper discusses microphysical simulation of interactions in liquid xenon, the active detector medium in many leading rare-event physics searches, and describes experimental observables useful to understanding detector performance. The scintillation and ionization yield distributions for signal and background are presented using the Noble Element Simulation Technique, or NEST, which is a toolkit based upon experimental data and simple, empirical formulae. NEST models of light and of charge production as a function of particle type, energy, and electric field are reviewed, as well as of energy resolution and final pulse areas. After vetting of NEST against raw data, with several specific examples pulled from XENON, ZEPLIN, LUX / LZ, and PandaX, we interpolate and extrapolate its models to draw new conclusions on the properties of future detectors (*e.g.*, XLZD), in terms of the best possible discrimination of electronic recoil backgrounds from the potential nuclear recoil signal due to WIMP dark matter. We find that the oft-quoted value of a 99.5% discrimination is likely too conservative. NEST shows that another order of magnitude improvement (99.95% discrimination) may be achievable with a high photon detection efficiency ($g_1 \sim 15 - 20\%$) and reasonably achievable drift field of ≈ 300 V/cm.

Keywords: WIMP dark matter direct detection, 2-phase LXe TPCs, simulations / models

I. INTRODUCTION

For the past ~ 15 years, the leading results from dark matter searches labeled as “direct detection” have come from detectors based on the principle of the dual-phase TPC (Time Projection Chamber) using a liquefied noble element as a detection medium [1]. Detectors filled with liquid xenon (LXe) have in particular produced the most stringent cross-section constraints, for spin-independent (SI) as well as neutron spin-dependent (SD) interactions between WIMPs (Weakly Interacting Massive Particles) and xenon nuclei. More recently, usage of LXe has also led to WIMP limits using different EFT (Effective Field Theory) operators, for mass-energies above $O(5 \text{ GeV})$ [2]. EFTs extend the set of allowable operators beyond the standard SI and SD interactions, and include searches at

higher nuclear recoil energies. Unrelated to dark matter, electron-recoil searches up to the MeV regime have set strict constraints on $0\nu\beta\beta$ decay [3], and have led to the observation of Xe DEC (double electron capture) [4].

To interpret results from past, present, and future experiments, a reliable MC (Monte Carlo) simulation is one necessity. Recent works have demonstrated the utility of NEST, the cross-disciplinary, detector-agnostic MC software used here [5–8], for a variety of active detector materials such as LAr [9, 10] and GXe, but especially LXe. As multi-tonne-scale TPCs have commenced data collection, improved MC techniques will not only assist in limit setting, but will be needed to extract dark matter particle mass and cross section in the event of a WIMP discovery. In either scenario, or in the design of a new TPC, predictions of performance are needed on key metrics such as dark matter signal discrimination from electronic recoil background in LXe, the focus of this work. NEST v2.4 is its default, but older versions are specified when needed.

* Corresponding Author: mszydagis@albany.edu

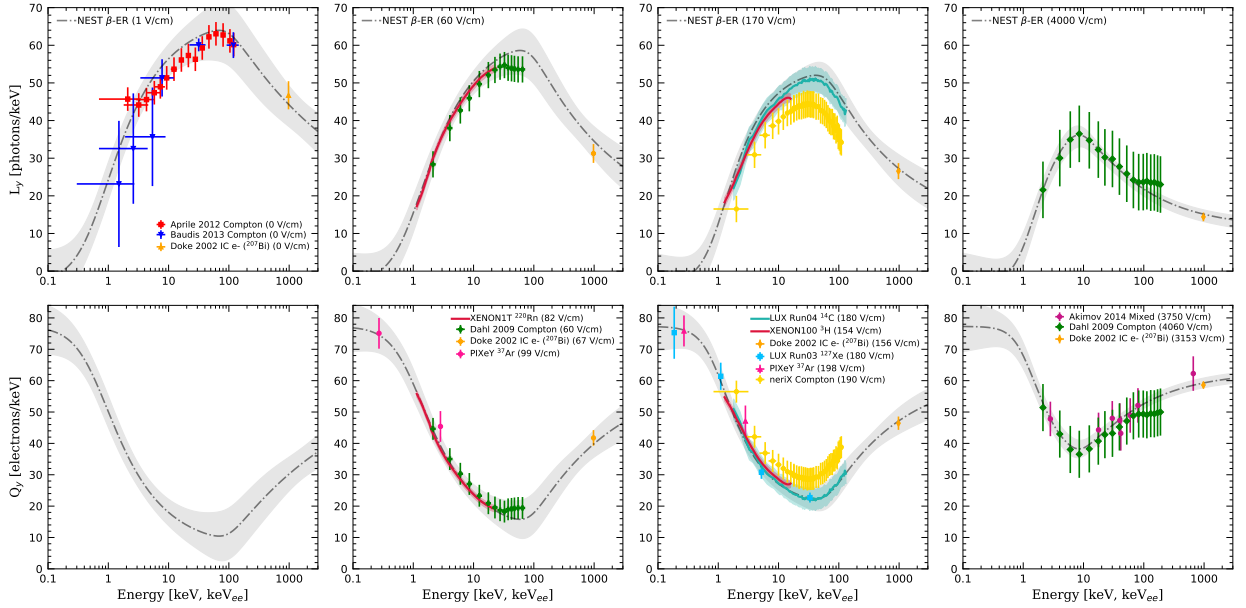


FIG. 1. β electron recoil (ER) L_y (top row) and Q_y (bottom) vs. energy E . Different fields \mathcal{E} are represented, from 0 V/cm at left to the highest fields for which data exist at multiple E s, ~ 3 -4 kV/cm, at right. More data exist, all of which are utilized to inform NEST, but these are selected as representative examples of the lowest and highest \mathcal{E} s and lowest and highest E , from sub-keV to 1 MeV across different types of experiments [11–21]. MC lines are black dashed with gray 1σ error bands. Newer results *e.g.* XENON1T’s ^{220}Rn calibration illustrate the predictive power of NEST, using the latest β model. It stems from ^{14}C [17, 22] but was also fit to Compton scatters, which may differ. Evidence for that is modest, and we treat them identically.

II. MICROPHYSICS MODELING EVALUATION

NEST model choices were justified earlier ([23] and in references therein) but are re-evaluated herein as foundations for reproduction of discrimination. NEST is openly shared, allowing it to be updated regularly with the latest data [24]. While data sets often provide relative light and charge yields, these are converted to absolute yields if the detector gains are calculable. Uncertainties in these gains are a significant source of systematic uncertainty, but newer data from higher-quality calibrations mitigate this. Combining calibration data ranging from < 1 keV to > 1 MeV energy, NEST has predictive shapes for primary scintillation and ionization yields as a function of energy E and drift electric field \mathcal{E} for different particle interaction types, including the decrease in light yield and increase in charge yield as \mathcal{E} increases [25]. The status of the NEST modeling of these shapes is shown in Figure 1.

A. Electronic Recoils (Betas, Gammas, X Rays)

NEST begins with a model of total yield, summing the VUV (vacuum ultraviolet) scintillation photons and ionization electrons produced. IR photons are not included, because the yield in LXe is low [26] and the wavelength is beyond the sensitivity of photon sensors in common use. The work function W_q for production of quanta depends only upon the density, with a simple (linear) fit based on data collected in [27], across solid, liquid, and gas:

$$W_q [eV] = 21.94 - 2.93\rho. \quad (1)$$

ρ is mass density in units of g/cm^3 . LXe TPCs typically operate at temperatures of 165-180 K and pressures of

1.5-2 bar(a), leading to $\rho \approx 2.9 \text{ g}/\text{cm}^3$ and resulting in a W_q of between 13-14 eV [28]. The exciton-ion ratio will determine how generic quanta break down into excited atoms, *i.e.* excitons N_{ex} , versus pairs of ionized atoms with freed electrons N_i :

$$N_{ex}/N_i = (0.0674 + 0.0397\rho) \times \text{erf}(0.05E), \quad (2)$$

where E is deposited energy in keV, for a beta interaction or Compton scatter. Here the ρ dependence is based again on [27] while the E dependence comes from reconciling [29–31], given evidence that light yield approaches zero as energy E decreases. Ionization electrons can recombine with Xe atoms or escape, given the presence of a drift field. So the number of photons N_{ph} is not simply equal to N_{ex} . This is the source of anti-correlation, motivating the use of both charge and light to measure the energy, $E = W_q (N_{ph} + N_{e^-})$ [23]:

$$\begin{aligned} N_{ph} &= [N_{ex} + r(E, \mathcal{E}, \rho)N_i] \propto S1 \\ N_{e^-} &= [1 - r(E, \mathcal{E}, \rho)]N_i \propto S2, \end{aligned} \quad (3)$$

where r is recombination probability for e^- -ion pairs depending on E , \mathcal{E} , and ρ , as well as particle and interaction type, and the S1 and S2 are the experimental observables (defined in Section III A). An experiment most commonly quotes results as specific light and charge yields per unit keV, L_y and Q_y , defined as N_{ph}/E and N_{e^-}/E .

Q_y is modeled first; L_y is set by W_q and subtraction:

$$\begin{aligned} N_q &\equiv N_{ex} + N_i = N_{ph} + N_{e^-} = E / W_q, \text{ where} \\ N_{e^-} &= Q_y E, \text{ and} \\ N_{ph} &= N_q - N_{e^-}. \end{aligned} \quad (4)$$

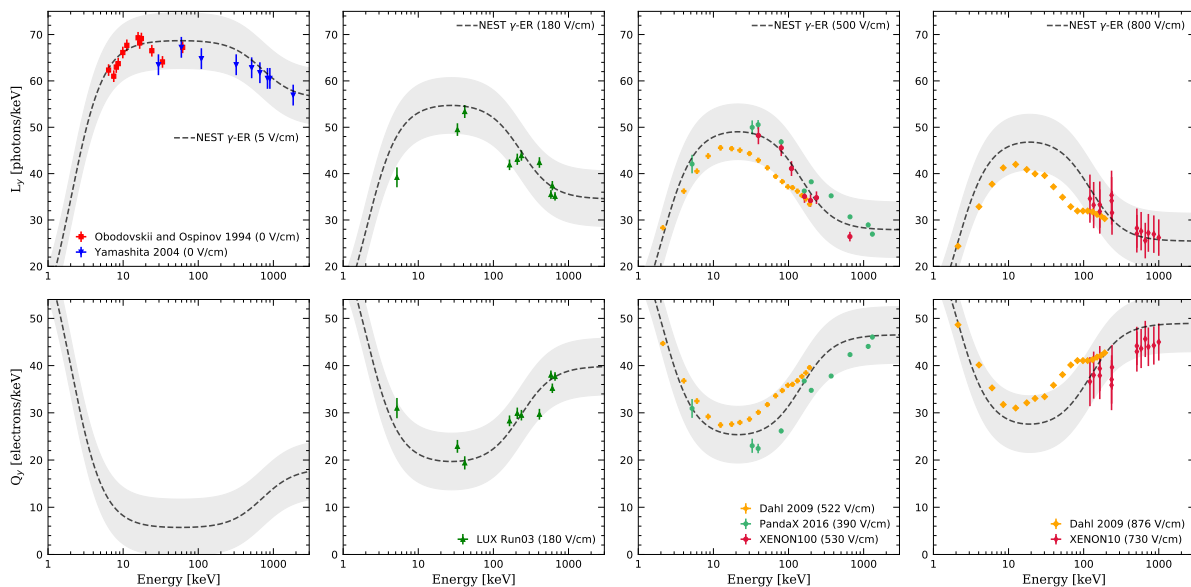


FIG. 2. γ ER L_y (top) and Q_y (bottom) vs. E at $\mathcal{E} = 0$ (left) to nearly 10^3 V/cm (right). Before β calibrations were common, photoabsorption peaks from monoenergetic γ s were used [15, 32–37]. At sufficiently high E , L_y is lower and Q_y higher than in Fig. 1, as some multiple scattering below position resolutions occurs, treated as single scattering in NEST: multiple lower- E , higher- dE/dx vertices are “averaged over.” Now x is true (γ) E even for data. Low fields again approximate 0 V/cm, when NEST becomes singular. As in other plots gray 1σ bands are driven by data errors, model shape constraints (sigmoidal), and monotonic \mathcal{E} dependence. LUX L_y points but not Q_y seem systematically low due to a different W_q used, with LUX assuming 13.7 eV (no ρ dependence). Dahl data sets exhibit different shapes due to being mixtures of Comptons and photoabsorption.

N_q is the total quanta, and N_{ph} is also $L_y E$. This procedure leverages the greater reliability of S2 measurements *cf.* S1 for lower E , as explained in [19, 23]. Q_y in the ER (electron recoil) model is a sum of two sigmoids:

$$Q_y(E, \mathcal{E}, \rho) = m_1(\mathcal{E}, \rho) + \frac{m_2 - m_1(\mathcal{E}, \rho)}{\left[1 + \left(\frac{E}{m_3}\right)^{m_4}\right]^{m_9}} + m_5 - \frac{m_5}{\left[1 + \left(\frac{E}{m_7(\mathcal{E})}\right)^{m_8}\right]^{m_{10}}}, \quad (5)$$

with m_1 serving as basic, field- / mass-density-dependent level. A fixed m_2 determines low- E behavior, while m_7 controls the field-dependent (\mathcal{E}) shape at high Es . These and all ms are empirically determined but the others are constant in \mathcal{E} [22]. (m_6 is not present, as it would create a degeneracy.) That being said, the first and second lines of Equation 5 together capture the behavior from two first-principles options – the Thomas-Imel box model at low E [38] and Doke-modified Birks Law at high E [39]. Microphysics above ~ 15 keV involves cylinder-like tracks. Because of where these Es lie along the Xe Bethe-Bloch curve, dE/dx decreases with increasing E , and, as a result, the recombination probability r and in turn L_y decreases, increasing Q_y [40–42]. Low- E deposits are more amorphous, with straight 1D track lengths becoming ill-defined: r and L_y instead increase with the 3D ionization density and E , as dE/dx instead increases with E .

r is found retroactively in recent NEST versions after fitting to Q_y per Equation 5, chosen to match both the box and Birks models. Using Equation 2 as a constraint avoids the degeneracy of r with N_{ex}/N_i , with the sum $N_{ex} + N_i$ (also equal to $N_{ph} + N_{e^-}$) already constrained by Equations 1 and 4: the former determines W_q and

the latter total quanta N_q based upon W_q . A raising or a lowering of W_q (one work function averaging over individual work functions for photon and electron production) should change L_y and Q_y equally, preserving both their shapes in both E and \mathcal{E} [43].

Figure 1 summarizes both L_y and Q_y from both data and NEST, at $\rho = 2.89$ g/cm³ ($T = 173$ K, $P = 1.57$ bar) for β s interacting as well as Compton scatters. This is a typical LXe operational point. The non-monotonic E dependence is clear. Meanwhile, the L_y decreases from left to right (top) and Q_y correspondingly increases (bottom) as \mathcal{E} increases, suppressing recombination but keeping N_q fixed. But even at $\mathcal{E} = 0$ there exists a “phantom” Q_y , as explained in [13, 23]. It is not observable in data, except by noting L_y vs. E is the same shape at all \mathcal{E} s, even 0. That implies a continuous change in L_y as $\mathcal{E} \rightarrow 0$. Non-zero fields standing in for 0 represent residual stray fields in a detector and/or the inherent fields of Xe atoms [44].

Absorption of any high- E photon, a γ or x-ray, is modeled like β interactions and Compton scatters, but with unique ms (Figure 2), to capture sub-position-resolution multiple scatters and distinct dE/dx . While the γ and β models might be merge-able using dE/dx , γ s are treated independently at present. Appendix A lists the β and γ model parameters, and those for nuclear recoil (NR).

B. Yield Fluctuations

Energy resolution typically refers to Gaussian widths (σ or FWHM) of monoenergetic peaks from high- E γ -ray photoabsorption, but it is also relevant to lower Es , in WIMP searches. Smearing of continuous ER spectra can drive an increase in signal-like background events. But to

understand statistical limitations on high-level parameters like monoenergetic peak σ or background discrimination we must start with lower-level parameters behind all the relevant stochastic processes involved. This modeling is discussed in depth in [23] but portions germane to this work are summarized here.

Realistic smearing of mean yields begins with a Fano-like factor F_q applied to total quanta N_q prior to differentiation into N_{ex} vs. N_i . It is labeled as Fano-like, as it does not follow the strict sub-Poissonian definition [45]. F_q may exceed 1, but is still used in the usual definition of the standard deviation of N_q , namely:

$$\sigma_q = \sqrt{F_q \langle N_q \rangle}, \quad (6)$$

where F_q is defined for light and charge together as

$$F_q = 0.13 - 0.030\rho - 0.0057\rho^2 + 0.0016\rho^3 + 0.0015\sqrt{\langle N_q \rangle}\sqrt{\mathcal{E}}. \quad (7)$$

The first line of Equation 7 is a spline of mass-density-dependent data [27] to allow for gas, liquid, or solid. The constant 0.13 represents the theoretical value of the Fano factor in Xe following the traditional definition ($F_q < 1$) and also matches NEXT gas data [46]. The second line of Equation 7 applies only to liquid Xe and is data-driven. The $\sqrt{N_q}$ term is included in order to match the data at MeV scales (*e.g.*, in $0\nu\beta\beta$ searches). Such results did not achieve the theoretical minimum in E resolution even if reconstructing N_q , utilizing both channels of information (light and charge), instead of only a single channel. This was true even for cases where the noise was allegedly subtracted or modeled [47, 48]. The $\sqrt{\mathcal{E}}$ term forces F_q to increase with \mathcal{E} . When \mathcal{E} increases, Q_y , already the greater contributor to quanta, increases, causing an improvement in the combined- E resolution. However, it is smaller than naively predicted, so the field term decreases the rate at which resolution improves, to match the data [49, 50].

There are many possible explanations for F_q becoming $\gg 1$ as E or \mathcal{E} changes. W_q may need to be replaced with separate values for the excitation and ionization processes (both inelastic scattering), then further subdivided into different values that depend upon e^- energy shell. Lastly, elastic scattering of orbital e^- s may play a role. Mechanisms are discussed in [51] but explicit Fano-factor variations can be found in [23].

In NEST a Gaussian smearing is applied to N_q having the width defined by Equation 6. A binomial distribution is then used to divide quanta into excitons and ions in type, following Equation 2.

F_q drives resolution on a combined- E scale, but such a scale is more relevant for monoenergetic peaks than within a WIMP search [15, 23]. The ‘‘recombination fluctuations,’’ however, describe variations and co-variations around the means of Equations 2,3,4. These fluctuations are canceled out with a combined- E scale, but constitute one of the key factors for characterization of ER discrimination [52]. These are fundamental and do not originate

from detector effects [34, 37]. Moreover, they are not binomial, despite recombination (or, escape) appearing to be a binary decision. Potential explanations for this phenomenon include other energy loss mechanisms, or other variables which break the independence of draws [53–56].

While it is unclear which explanation is correct, NEST proceeds with a fully empirical approach to simply model what is observed in data; following [22, 34] closely, NEST defines the variance in the recombination to be:

$$\begin{aligned} \sigma_r^2 &= \langle r \rangle (1 - \langle r \rangle) N_i + \sigma_p^2 N_i^2, \text{ where} \\ \sigma_{e^-} &= \sigma_{ph} = \sigma_r, \\ \sigma_p &= A(\mathcal{E}) e^{-\frac{((y) - \xi)^2}{2\omega^2}} [1 + \text{erf}(\alpha_p \frac{(y) - \xi}{\omega\sqrt{2}})], \end{aligned} \quad (8)$$

and the electron fraction $y = N_{e^-}/N_q$.

The $\langle r \rangle (1 - \langle r \rangle) N_i$ in σ_r follows the binomial expectation of $\sigma_r \propto \sqrt{N_i}$. The σ_p term leads to $\sigma_r \propto N_i$, as proposed in [52]. σ_p is a skewed Gaussian (on the third line), with an amplitude A depending on \mathcal{E} , varying from 0.05-0.1, as needed to simulate the increase in widths of the ER band with higher field [22, 57]. In NEST versions < 2.1 , σ_p was simulated as a constant, similar in value to A , but a constant is inadequate for capturing the full behavior of recombination fluctuations [34].

Instead of $\langle r \rangle$, σ_p 's dependent variable was chosen as N_{e^-} fraction $\langle y \rangle$, closely related to $1 - \langle r \rangle$. It is simpler and leads to a better fit to data. Recombination probability, defined within Equation 3, is degenerate with N_{ex}/N_i , while y is directly measurable. It can be written in terms of r : $y = (1 - r)/(1 + N_{ex}/N_i)$ [15]. Non-binomial fluctuations decrease as $y \rightarrow 1$ or $y \rightarrow 0$, as $\sigma_p \rightarrow 0$. ξ , ω , and α_p are the centroid, width, and skew of σ_p , respectively. Default NEST values are $\omega = 0.2$, determining the width of σ_p , and $\alpha_p = -0.2$, setting its skewness. (Future work may recast all of σ_r entirely in terms of y , not just σ_p .)

$\xi \approx 0.4 - 0.5$ was found based upon beta and gamma-ray ER data. The types of data utilized were band widths and monoenergetic peak energy resolutions, both at multiple \mathcal{E} s and E s [15, 37, 52]. ξ 's value depends on what data sets are used and what other parameters are fixed. A ξ near 0.5 leads to a maximum in σ_p (within σ_r) near $y = 0.5$, as would occur within a regular binomial distribution, wherein r is multiplied by $(1 - r)$, as in the first term of σ_r^2 in Equation 8. The asymmetry which stems from the choice of a skew-normal in place of a normal function for σ_p allows for matching data where lower y , which occurs at high E s or at low \mathcal{E} s, exhibits different fluctuations compared to higher y . High y occurs at low E s and high \mathcal{E} s, *i.e.* greater N_{e^-} and Q_y [22, 52, 58].

The skew Gaussian $\sigma_p(y)$ must not be conflated with the E and \mathcal{E} -dependent skew defined in Section IVB of [57] as α_r , which is not just a convenient fit to an internal variable like α_p , but manifests itself as asymmetry in N_{e^-} , which is generated not from a normal but a skew-normal distribution, of the same form as Equation 8's. The mean $N_{e^-} = (1 - r)N_i$ is smeared using σ_r , but was

not skewed in NEST before v2.1. N_{e-} skew α_r as defined by Equation (13) in [57], unrelated to α_p , is applied after it. At typical \mathcal{E} s and WIMP-search E s, it is $\gtrsim 2$.

Later we will see a positive α_r value can lead to better background discrimination than expected for LXe. Weak rejection was expected due to the recombination fluctuations being greater (worse) than binomial, but positive α_r will shift ER events preferentially away from NR (more Q_y). This has already been observed [57].

Lastly, while σ_q leads to correlated change in S1 (L_y) and S2 (Q_y), and σ_r to anti-correlated change, uncorrelated noise also exists, affecting S1 and S2 differently. S1 and S2 gains are understood sources, assuming position-dependent light collection and field non-uniformities are taken into account. Unknown sources are modeled with a Gaussian smearing proportional to the pulse areas [28]. A quadratic term may be necessary at the MeV scale [56]. ER and NR are equally affected by any detector effects (known/unknown). Final E resolutions vs. E are seen for ER, NR, or both in [5, 28], supplementing validation of means in our Figs. 1-3 with their vetting of fluctuations. The scale of the unknown detector effects across experiments is 1-10% [23, 28, 79] (for S2; 0% for S1 spike count).

C. Nuclear Recoils (Neutrons and WIMPs)

NR N'_q (differentiated in this section from ER with a prime) is well fit by a power law across >3 orders of magnitude in E (Fig. 5 in [23]). This is a simplification of the Lindhard approach to modeling the reduced quanta compared with ER, but also allows for departures from Lindhard at higher E s, lowering $N'_q(E)$'s slope in log space with respect to Lindhard. Fewer equations and parameters are involved compared to Lindhard, which is a combination of multiple power laws inside of a rational function [80]: see Eqn. 8 in [23]. NEST instead uses:

$$N'_q = \alpha E^\beta, \text{ where } \alpha = 11_{-0.5}^{+2.0} \text{ and } \beta = 1.1 \pm 0.05. \quad (9)$$

The uncertainties here are $>10x$ those reported recently for the same fit, as only statistical error was included in Eqn. 6 of [23]. Here, systematic uncertainties in S1 detection efficiency and S2 gain (including e^- extraction efficiency) are included. They can be found in the individual references in the Figure 3 caption. Individual power laws were found for each data set prior to an error-weighted combination, so that a data set with more points was not overly weighted. Equation 9 was also cross-checked with the L'_y and Q'_y individually extracted from data as displayed in Figure 3, and raw S2 vs. S1 band data.

Equation 9 can be used to define \mathcal{L} , *i.e.* quenching:

$$\mathcal{L}(E, \rho) = N'_q(E) / N_q(E, \rho) = N'_q(E) W_q(\rho) / E. \quad (10)$$

\mathcal{L} permits one to define the electron equivalent energy in units of keV_{ee} for NR, as $\mathcal{L} \times (E \text{ in } \text{keV}_{nr})$, a best average reconstruction of the (combined-) E of recoiling nuclei. This \mathcal{L} should be applicable to neutron calibrations, WIMPs, and $\text{CE}\nu\text{NS}$, such as from ^8B nuclear fusion [7].

The next equation combines N_{ex}/N_i with recombination probability, as their effects are degenerate. While the previous equation set total quanta, this one determines division into the individual yields (charge or light) in an anti-correlated fashion, reducing r with higher \mathcal{E} , as the exponent for the drift field is negative.

$$\varsigma(\mathcal{E}, \rho) = \gamma \mathcal{E}^\delta \left(\frac{\rho}{\rho_0} \right)^v, \text{ where } \gamma = 0.0480 \pm 0.0021, \\ \delta = -0.0533 \pm 0.0068, \text{ and } v = 0.3. \quad (11)$$

The reference density $\rho_0 \equiv 2.90 \text{ g/cm}^3$. The exponent v for the density dependence is hypothetical. It is not well measured at densities significantly deviating from ρ_0 [15].

We utilize Equation 11 to produce a Q'_y equation:

$$Q'_y(E, \mathcal{E}, \rho) = N_{e-} \text{ per keV} = \\ \frac{1}{\varsigma(\mathcal{E}, \rho)(E + \epsilon)^p} \left(1 - \frac{1}{1 + (\frac{E}{\zeta})^\eta} \right), \text{ where} \\ \epsilon = 12.6_{-2.9}^{+3.4} \text{ keV}, \quad p = 0.5, \\ \zeta = 0.3 \pm 0.1 \text{ keV}, \text{ and } \eta = 2 \pm 1. \quad (12)$$

Energy deposited is again E (in keV), while epsilon (ϵ), also an energy, is the reshaping parameter for the E dependence. Higher or lower ζ lowers or raises the Q'_y level respectively, providing the (E -)field dependence. ϵ can be thought of as the characteristic E where the Q'_y changes in its behavior from \sim constant at $O(1 \text{ keV})$ to falling at $O(10 \text{ keV})$. (Note ζ has adaptable units of keV^{1-p} .)

ζ and η are the two sigmoid parameters that control the Q'_y roll-off at sub-keV energies. They permit a better match to not only the most recent calibrations [68, 72], but also to NEST versions pre-2.0, and other past models. Lindhard (Eqn. 8 of [23]) if combined with Thomas-Imel recombination (Eqn. 15 of Section II D) has a roll-off but less steep than data, or NEST v2.2+ [44, 75]. η controls steepness, while ζ represents a characteristic scale for NR to remove one e^- [23, 81]. At high E , $p = 0.5$ reproduces $Q'_y \propto 1/\sqrt{E}$ (Figure 3, bottom row).

N_{ph} is derived from $N'_q - N_{e-}$, as for ER, but this is only a temporary anti-correlation enforcement, as then a sigmoid of the same type as the second half of Q'_y (Equation 13) permits L'_y 's flexibility. Future calibration data could show a drop, or even flattening potentially, due to additional N_{ph} from the Migdal effect [67, 82]. An L'_y increase is possible even as $E \rightarrow 0$. This is not unphysical as long as N_{ph} vanishes in that limit, conserving E .

$$L''_y = \frac{N'_q}{E} - Q'_y. \\ N_{ph} = L''_y E \left(1 - \frac{1}{1 + (\frac{E}{\theta})^\iota} \right); \quad L'_y = \frac{N_{ph}}{E},$$

where $\theta = 0.3 \pm 0.05 \text{ keV}$ and $\iota = 2 \pm 0.5$.

$$N'_q = N_{ph} + N_{e-}. \quad (13)$$

The top row of Figure 3, especially if read from right to left, shows the same L'_y shape at all fields, indicative once again of a zero-field phantom Q'_y . In the L'_y calculation,

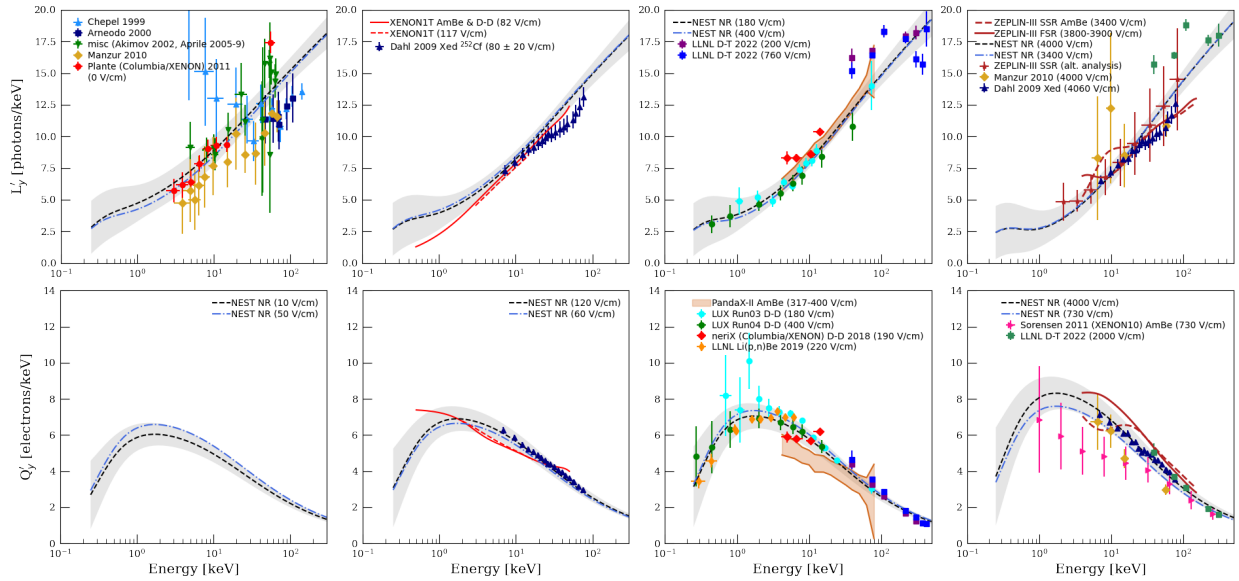


FIG. 3. L'_y (top) and Q'_y (bottom) vs. E , from $\mathcal{E} = 0$ V/cm at left to the highest \mathcal{E} for which data exist at right [6, 14, 15, 59–74]. Newer works from XENON1T and PandaX were not included in fits (yet agree at the 1- 2σ level). NEST lines are blue and black, at similar \mathcal{E} s. Uncertainties on NEST increase as $E \rightarrow 0$ or ∞ , as the amount of data decreases at each extreme. \mathcal{E} dependence is weaker compared with ER (Figure 2). Summing L'_y and Q'_y results in a power law, not a constant (ER), and $N'_q < N_q$ [23, 75]. For systematically-offset data sets, our fit can average them if they share the same qualitative trend. Discrepant results sharing the same trend point towards a systematic offset in the S1 and/or S2 gains, with the S1 most affected by the 2-PE effect [76] and the S2 affected by assuming 100% e^- extraction prior to more recent measurements [77, 78]. Only Chepel 1999 L_y (upper left) is excluded from the fits used to tune NEST. As NR dE/dx decreases with decreasing E , e^- escape probability increases, causing L'_y to decrease. (L'_y 's shape is also determined by the \mathcal{L} -factor.) For Q'_y , there is a maximum, as the \mathcal{L} -factor decreases and $(1-r)$ increases as $E \rightarrow 0$, at different rates. In contrast to [23], where the focus was \mathcal{L} , we separate L'_y and Q'_y here. While the errors imply no \mathcal{E} dependence, when data are taken in one detector at many \mathcal{E} s, a rising Q'_y (falling L'_y) with \mathcal{E} is clear [15].

L''_y is a temporary variable (perfect anti-correlation) used within NEST to calculate the final L'_y and N'_q . The best-fit numbers for θ and ι match those of their counterparts ζ and η for Q'_y . In this modular but smooth approach the sigmoidal terms in L'_y and Q'_y go to 1.0 with increasing E . In this fashion it is possible to fit the low- and high- E regimes separately, allowing for a possibility that different physics occurs in the sub-keV region, to avoid use of higher- E data to over-constrain lower- E yields.

The two sigmoids lower the predictive power of NEST for extrapolation into newer, lower- E regimes where no calibrations exist. In the case of L'_y , it will be challenging to achieve any, at least with reasonable uncertainty.

θ is a physically-motivated characteristic E for release of a single (VUV) photon. Like ζ , its value is 300 eV, in agreement with Sorensen [81], and NEST pre-v2.0.0 [44]. Fundamental physics models, such as Lindhard [80] and Hitachi [83, 84] for the \mathcal{L} governing total quanta, coupled to the Thomas-Imel “box” model for recombination [38], predict a similar value. Larger θ means more E is needed to produce a single photon (as opposed to excitons) potentially detectable for an experiment, depending upon the light collection efficiency. It means a lower L'_y .

$\iota \rightarrow 0$ would lower L'_y as well and for a value of exactly 0 the reduction in L'_y is a factor of two across all E . On the other hand, in the limit of infinite ι (and/or $\theta \rightarrow 0$) the effect of the sigmoid is entirely removed, raising L'_y at low E . The same is true for η and ζ in the Q'_y formu-

lation. A hard cut-off for any quanta was implemented in NEST for $E < W_q$ (N_q / N'_q) ≈ 200 eV. N_q represents the quanta which would have been generated for same- E ER. Below this, no quanta are generated at all. Sub-keV recoils have been observed at 200-400 V/cm (Figure 3).

In contrast to ER, simulated $\langle N'_q \rangle$ is not varied with a common Fano factor shared by both types of quanta. For NR, there are (nominally) separate Fano factors for the excitation and ionization which can soften the strict anti-correlation at the level of the fundamental quanta. $\langle N_{ex} \rangle$ is smeared using a Gaussian of standard deviation $\sqrt{F_{ex} \langle N_{ex} \rangle}$. $\langle N_i \rangle$ is similarly varied, using $\sigma = \sqrt{F_i \langle N_i \rangle}$, as is standard practice for Fano factors [85]. Based upon the sparse existing reports of NR E resolution [67, 72, 86] both F_{ex} and F_i are set to 1 in NEST (as of v2.3.10).

Using the same functional form as in Equation 8 from ER, NEST models fluctuations in recombination for redistribution of photons and electrons prior to measurable NR S1 and S2. The new parameters are distinguished using a prime superscript again.

Parameter values are similar but not identical to those from ER: $A' = 0.10$ (fixed for all fields), $\xi' = 0.50$, and $\omega' = 0.19$ ($\alpha'_p = 0$). These set a final recombination width σ'_r . N_{e-} and N_{ph} distributions have that width but are also skewed ($\alpha'_r = 2.25$), leading to NR band asymmetry. α'_r may be higher, but it is difficult to disambiguate NR band skew in data from unresolved multiple scatters or other detector effects [57], or from the Migdal Effect [87].

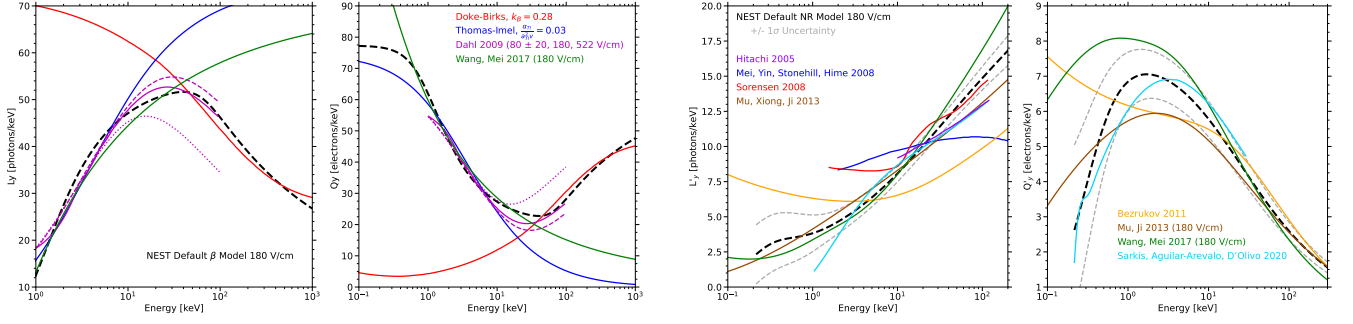


FIG. 4. Comparing NEST with other approaches: L_y (a,c) and Q_y (b,d) alternate, for ER (a,b) and NR (c,d), at 180 V/cm [15, 29, 38, 88]. The second legend applies to both the first and second plots. This was LUX’s initial field [89], in between XENON1T at 80 [90] and earlier works like [37] as high as 730 V/cm. While similar to fundamental approaches, NEST incorporates features of multiple, splitting differences and following the data. The Thomas-Imel (T-I) and Doke/Birks sample curves shown are meant to match 180 V/cm the most closely. Unlike the T-I and plasma models, NEST accounts for the high- E (low- dE/dx) L_y decrease (Q_y increase) [88]. Birks does too, but fails to work at low E s (high dE/dx) [91]. Dahl presented variations on T-I, utilizable for high E s by breaking up tracks into boxes, although his closest fields were 80 and 522 V/cm [15]. We show a 180 V/cm model (solid), *i.e.*, a weighted average of his 80 (dashed) and 522 V/cm (dotted) models. There are more NR models (right), due to a need to explain potential WIMPs [83, 88, 92–97]. Older models based on L_{eff} , which was L'_y relative to ^{57}Co γ -rays (122 keV), were translated assuming 64 photons/keV at 0 V/cm with a small error [41, 98] unless papers had a different value, which we then used instead (Bezrukov: 53). If they presented multiple models, we plot the most central one and/or one closest to data. Comparisons are only qualitative here, ensuring NEST has the correct, physically-motivated shape across different regimes.

D. Comparisons to First-Principles Approaches

By smoothly interpolating data taken at individual energies and/or fields, NEST is now fully empirical, built on sigmoids and power laws as needed for a continuous model. But inherent uncertainty is introduced by extrapolating into new E or \mathcal{E} regimes. To assess that, and further validate an empirical approach, we show agreement to the models closer to “first principles.” Within NEST’s earliest versions, the Thomas-Imel (T-I) box model [38] was used for low E , while for high E Birks’ Law of scintillation was adopted. The latter was similar to the Doke approach [41] for scintillation alone, but applied here to recombination directly so it can model both L_y and Q_y :

$$\langle r \rangle = \frac{k_A \frac{dE}{dx}}{1 + k_B \frac{dE}{dx}} + k_C, \text{ with } k_C = 1 - k_A/k_B. \quad (14)$$

This is Birks’ Law from other scintillators [91], but with an additional constant k_C that accounts for parent-ion recombination [29]. Its constraint ensures $\langle r \rangle$ is between 0-1, as it is a probability. A best fit to ER (γ) data has a non-zero k_C only at 0 V/cm; at non-zero \mathcal{E} , Equation 14 contains only one Birks’ constant, $k_A = k_B$.

k_B ’s best-fit value (for 180 V/cm) is 0.28, from a fit to only the high- E portion of the NEST beta model. That is in turn supported by data from LUX and XENON ^3H , ^{14}C , Rn. Notably, k_B in NEST v0.9x and the first NEST paper 12 years ago for this \mathcal{E} was 0.257 (see Figure 4).

Despite Birks’ great success in explaining data at high E , the “law” cannot capture the behavior of ER at $E \lesssim 50$ keV. While lower- E extensions are possible, such as addition of higher-order terms in dE/dx for that region, we instead consider the T-I model for lower E :

$$\langle r \rangle = 1 - \frac{\ln(1 + \xi_{TI})}{\xi_{TI}}, \text{ where } \xi_{TI} = \frac{N_i}{4} \frac{\alpha_{TI}}{a_{TI}^2 v_d}. \quad (15)$$

ξ_{TI} parameterizes the physical principles. α_{TI} describes diffusion, v_d is e^- drift velocity, and N_i is again number of ions. Diffusion is modeled using the relation $\alpha_{TI} = De^2/(kT\epsilon_d)$, where D combines e^- and positive-ion diffusion coefficients, e is the elementary charge, k is Boltzmann not Birks, T is temperature, and $\epsilon_d = 1.85 \times \epsilon_0$ is dielectric constant. $D = 18.3 \text{ cm}^2/\text{s}$ is the longitudinal diffusion constant for e^- s at 180 V/cm, derived from S2 pulse widths [99]. e^- diffusion dominates over cation diffusion. Assuming this D (and the $T = 173$ K as earlier), as well as $\epsilon_d = 1.85 \times \epsilon_0$, and taking $v_d = 1.51 \text{ mm}/\mu\text{s}$ at a $\mathcal{E} = 180 \text{ V/cm}$ [100], we find $\alpha_{TI} = 1.20 \times 10^{-9} \text{ m}^3/\text{s}$. From this, escape $1 - \langle r \rangle$ for e^- s inside a box is found by solving the relevant (Jaffé) differential equations [15].

We interpret a_{TI} (“box size”) as corresponding to a (\mathcal{E} -independent) e^- -ion thermalization distance of $4.6 \mu\text{m}$, as calculated by Mozumder [101]. This value was used before as a border in NEST for track length, to switch from T-I to Birks. The ultimate value of $\text{TIB} \equiv \alpha_{TI}/(a_{TI}^2 v_d)$ for that case is 0.0376.

Dahl found best-fit values of TIB ranging from 0.03-0.04 for both ER and NR data at 60-522 V/cm [15]. Our contemporary fits to NEST and to data, the blues lines at low energies in the first two plots at left in Figure 4, used 0.030. If v_d changes with drift field (it is typically $O(2 \text{ mm}/\mu\text{s})$ [102]), then the entire ranges of Dahl, and of Sorensen and Dahl, are covered: 0.02-0.05 [75].

For NR, one sees in Figure 4 (c, d) many different past models, mainly for L_y . NEST originally used T-I for NR, as Dahl / Sorensen [15, 75]. See the blue lines in Figure 5. It applies the same color convention as Fig. 4. While T-I fixes r , thus partitioning of E into L_y vs. Q_y , total yield must still be determined. For the maximal distinction, we have selected the original Lindhard formula for that, as laid out in multiple other works [23, 67, 75, 80], not

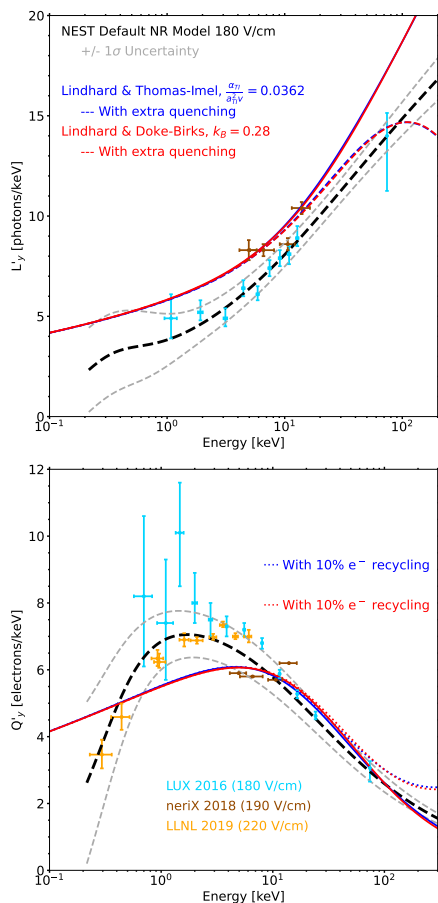


FIG. 5. The comparisons of NEST and selected NR data to only the Thomas-Imel box (blue) and Birks (red) models of recombination, always using Lindhard here to define N'_q (found as Eq. 8 in [23] and elsewhere). For L'_y , the dashed lines indicate additional quenching at higher E s and dE/dx , while for the Q'_y , where this quenching has no direct impact, the dotted lines indicate partial conversion of photons into e^- s from that effect (or not, solid lines). Some data, including at other fields, are consistent at a $1-2\sigma$ level with no quenching or conversion, not the amounts shown. The L'_y data from 50–100 keV $_{nr}$ are inconsistent: see Figure 3 upper left and [65].

Equation 9. We set the crucial Lindhard parameter $k_L = 0.166$, the decades-old default for Xe [80]. Averaging over E , $N'_q/N_q \approx k_L$. 0.166 is consistent with actual data [67], Lenardo’s meta-analysis [98], and NEST v2.3+.

We identify ς of Equation 12 with TIB value, as justified by Equation 11, wherein the parameters for the \mathcal{E} dependence of ς (γ and δ) overlap at the 1σ level with the power-law field dependence of TIB from [98]. At 180 V/cm, $\varsigma = 0.0362$, comparable to a best-fit TIB for ER, and quite close to our theoretical calculation earlier. We assumed NR $N_{ex}/N_i = 1.0$, higher than for ER, but the most common assumption for NR, with best fits to actual data as well as theory varying from 0.7-1.1 [75].

An additional quenching is applied to just L'_y [64]. We find a common parameterization of this effect [95] to be defined in a manner analogous to Equation 14:

$$q = \frac{1}{1 + \kappa \epsilon_Z^\lambda}, \quad \text{with } \epsilon_Z \sim 10^{-3} E, \quad (16)$$

where $q < 1$ is a multiplicative factor on L'_y . ϵ_Z is unitless reduced energy, useful for comparison between elements. Equation 16 is like 14. The power law can be identified as proportional to NR dE/dx . If we define dE/dx (or LET) as approximately $a\epsilon^\lambda$, then $\kappa = k_B a \mathcal{L}$. Assuming the ER k_B (defined as 0.28 for 180 V/cm in Figure 4b), $\mathcal{L} \sim 0.15$ (11/73) per an energy-independent approximation of Equation 9 justified by the power being close to 1, and $a = 100$, then $\kappa = 4.20$, $< 0.2\sigma$ away from [98]. A fraction of the quanta removed from L'_y in 16 may be convertible into Q'_y . Figure 5 bottom explores that with the fraction as 0.1.

Unlike with ER, Birks’ Law models NR over the entire E range of interest (Figure 5, red) with $k_B = 0.28$ and $dE/dx = a\epsilon^\lambda = 100\epsilon$. While there is disagreement about whether λ is 1.0 or 0.5 depending on the E regime [83, 84], 1.0 only differs by 1.6σ from the value of 1.14 in [98].

Looking back at alternatives to Lindhard, in Figure 4, we see NEST’s power law, L'_y , and Q'_y seem a good match for Mu and Xiong [94, 96], also for Wang and Mei [88, 92]. NEST’s lower 1σ line touches Sarkis’ L'_y [97], which is low due to not including the most recent points [67, 70]. On the high- E L'_y end, NEST’s upper uncertainty band encompasses neriX [71]. As for Q'_y , NEST lies in between [88] above and [96] and [97] below, falling in between LUX D-D [67] and LLNL [72].

The good agreement between the fully empirical NEST model and the first-principle models of both NR and ER shown here shows that NEST can accurately simulate the most likely dark matter signals and backgrounds, respectively. This should be the case even for the regimes where data are still lacking, or they exist but have large uncertainties. In the case of NR, the fully empirical approach reproduces all data better using a comparable number of free parameters, but much greater flexibility, compared to semi-empirical approaches. For fluctuations, the number of NEST free parameters increased, to two Fano factors (excitation, ionization) and four numbers for recombination width and skew, to fully model the E resolution.

In Sec. III, we transition to studying ER leakage into NR phase space, which has many axis options. Leakage is 1 minus discrimination, already explored by *e.g.* LUX [57] and XENON [18], but NEST, justified first using data, is not limited to where they exist to make predictions relevant for a future experiment. We also try to summarize / unify disparate approaches used by experiments, weighing advantages/disadvantages of plot aesthetics and ease of analytic fitting. L_y and Q_y must pass through a detector sim to obtain realistic S1 and S2 pulse areas, as per [103], with Equation 17 and binomials most important.

III. REPRODUCTION OF LEAKAGE

The discrimination of ER backgrounds from potential NR signals, such as dark matter WIMPs, requires care-

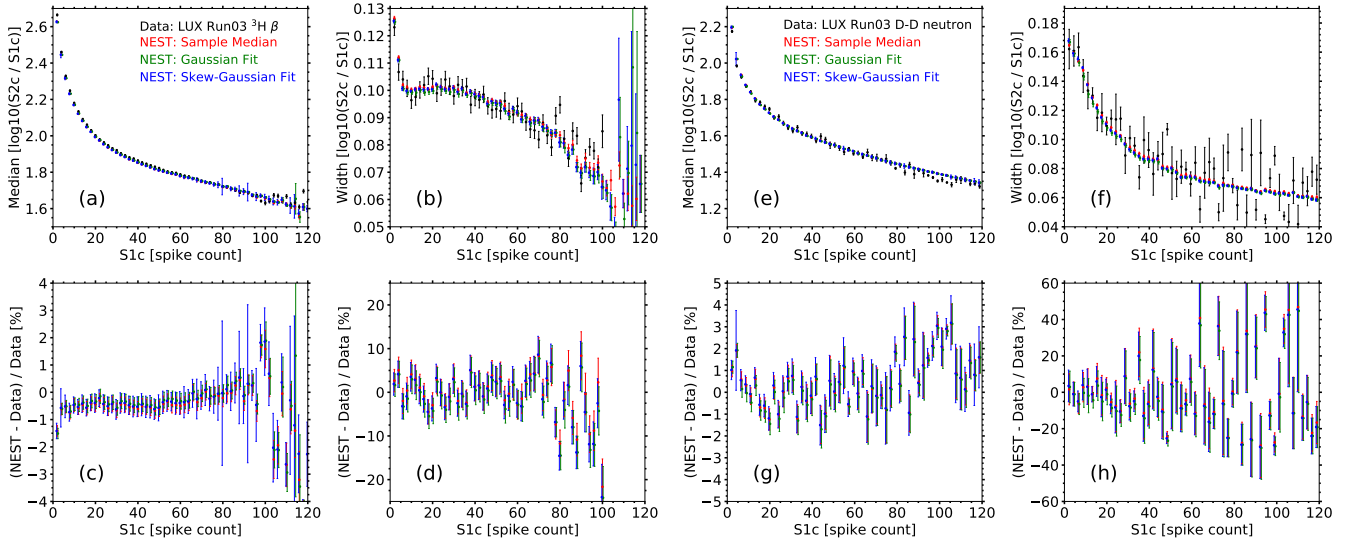


FIG. 6. Decomposition of ER (left plots: a-d) and NR bands (right: e-h) from LUX Run03 [100]. ER came from tritium (CH_3T *i.e.* tritiated methane) with a β -decay endpoint of 18.6 keV [30]. NR came from a deuterium-deuterium (D-D) fusion 2.4 MeV neutron gun, leading to Xe recoils up to 74 keV [67]. Plots (a,c,e,g) cover band medians and (b,d,f,h) the widths. The top row is overlays (a,b,e,f), bottom (c,d,g,h) percent differences between NEST and data normalized to data and lined up with the top by median and width. Different fit styles are indicated in red (no fit: sample median and standard deviation), green (Gaussian fits), and blue (skew) with data in black. Skew fits are better (Figure 7), but statistics drop at high S1 as a result of source E endpoints, and such fits are most affected due to the degeneracy caused by adding another free parameter. Percent deviations between model and data are typically an order of magnitude worse for widths compared to medians: they are more challenging to model (2nd order). But average deviations for $S1 < 100$ are typically $< 1\%$. 200,000 ^3H (tritium T) and 200,000 D-D events were simulated, matching the number of events in data in the former case, but 10x larger in the latter for easier fitting. In both cases, the number of calibration events was overwhelming compared to any/all types of background events, like Rn ER [104].

ful calibrations with radioactive sources first, β s and γ rays in the former case, and neutrons in the latter case as representative of WIMPs [105]. As LXe has been used for decades, we opted for two (representative) examples: 180 V/cm LUX [100], and 730 V/cm in XENON10 [37]. Together, these cover possible \mathcal{E} s and photon detection efficiencies for present / future work. Leakage is a strong function of their values [18, 52, 57]. Moreover, LUX conducted many unique calibrations [17, 19, 30, 67, 89] and XENON10 was the first LXe TPC seeking WIMPs [37].

We begin with Figure 6, the thorough comparisons of NEST to LUX in the traditional parameter space for discrimination, defined as the (\log_{10}) ratio of the secondary to the primary scintillation pulse area vs. primary scintillation signal area [106]. The medians or means in this, $\log(S2/S1)$ vs. $S1$, serve as the first examples of μ_{ER} and μ_{NR} from Equation (1), with the sample or fit standard deviations as σ_{ER} or σ_{NR} (driven primarily by σ_r and σ'_r). The primary and prompt signal is $S1$ and the secondary the $S2$. These are related to the N_{ph} and N_{e^-} originally generated, and $N_{ph} = L_y(l)E$ and $N_{e^-} = Q_y(l)E$. For $S1$ there is a position-dependent photon detection efficiency \vec{g}_1 which is the combination of the geometric light collection with the quantum efficiencies of photo-sensors, like PMTs. \vec{g}_2 is the gain for e^- s generating electroluminescence in the gas stage at the top of a two-phase detector, and it is greater than 1 [107]. $S1$ and $S2$ are defined as:

$$S1 = N_{ph} \vec{g}_1(x, y, z) \text{ and } S2 = N_{e^-} e^{\frac{t_d}{\tau_e}} \vec{g}_2(x, y). \quad (17)$$

Measured \vec{g}_2 depends only on radial position not the e^- drift direction (z) in the field. z -dependence is handled by the exponential e^- lifetime correction τ_e . Drift time $t_d = \Delta z / v_d$. g_2 is equivalent to a product of e^- extraction efficiency (which depends on extraction field), the number of photons produced per e^- Y_e , and the $S2$ photon detection efficiency (g_1^{gas}) [22]. Y_e depends on GXe density, GXe gap size, and GXe field.

Calibrations enable position corrections for normalizing detector response to $x=y=0$, and to the liquid surface in z for $S2$ s [107]. This results in scalar values for the g_1 and g_2 , but they can still vary by measurement or fit. After correction for internal detector positions, $S1$ and $S2$ are often renamed to $S1_c$ and $S2_c$ [22] (alternatively, $cS1$ and $cS2$ [90]), but unsubscripted $S1$ and $S2$ can also mean final corrected values [89, 100]. Published values for LUX tritium and D-D runs are $g_1 = 0.115 \pm 0.005$ phd/photon and $g_2 = 12.1 \pm 0.9$ phd/ e^- [30], and $g_1 = 0.115 \pm 0.004$ and $g_2 = 11.5 \pm 0.9$ [67], respectively. The values needed for good fits in NEST, on both band means and widths, are $g_1 = 0.117$ (both), $g_2 = 12.9$ (tritium), and $g_2 = 12.2$ (D-D). These are all well within the uncertainties, with g_2 being the most relevant for setting y-axis levels in Figure 6. The uncertainties as well as the differences in calibration constants between different runs were included in

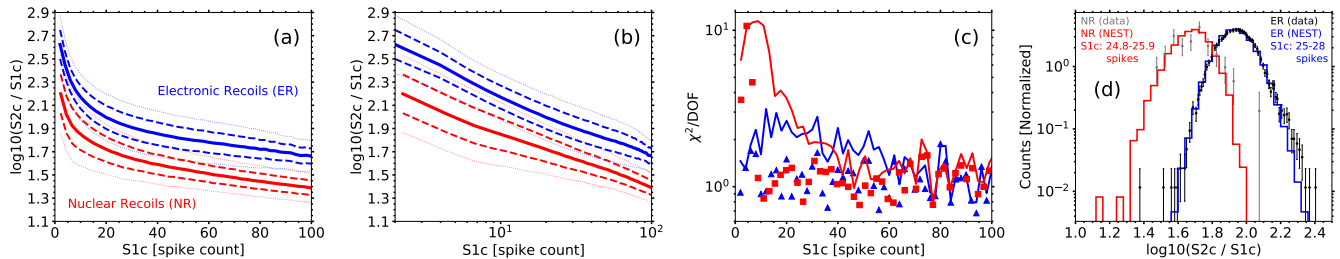


FIG. 7. (a) LUX band means and widths together illustrate how discrimination works. ER (blue, ${}^3\text{H}$) generates more ionization at a given amount of scintillation than NR (red, D-D). Thinner lines, dashed and dotted, represent $\pm 1-2\sigma$ on means. (b) The same data shown with a log-x axis better highlights the behavior at the lowest S1s and so lowest E_s . These are most important in a dark matter search for a WIMP of any mass, and show how a power-law or a log fit is inadequate. The solid lines in (a,b) are composed of centroids of fits to histograms for each bin. Those centroids are the individual points displayed in Figure 6 top row, the first and third plots (a,e). They can be well-fit by an offset hyperbola plus a line, $y' = m'_1/(S1+m'_2) + m'_3 S1 + m'_4$. m'_1 and m'_2 are $O(5)$, $m'_3 = O(-0.002)$, and $m'_4 = O(2)$. (c) χ^2/DoFs by bin from comparing data with NEST are in blue for ER, red NR. Lines stand for Gaussian fits, dots for skew fits. NR non-Gaussianity from a combination of single-S1-photon counting systematics with low S2s drives the first three red data points to high values, even for skew fits, which do not capture all non-Gaussianity. This is taken into account in later leakage calculations by considering differing definitions of NR band centroids. (d) Histograms of NEST and data for ER and NR serve as medium-S1 examples. These histograms are not collapsed as in (a,b) on the y axis to means and widths of fits. As they represent different S1 slices [30, 67], NR-ER overlap is worse than it would be at the same S1, and is an outlier in terms of agreement with NEST. The lowest ER data point is a significant outlier and assumed to be from a non-ER source. These histograms, with different binning, were the only choice for presentation, as the closest S1 bins for which published D-D and tritium histograms exist. The four distributions are normalized to unity separately.

the systematic errors calculated for LUX, as nuisance parameters within the PLR (Profile Likelihood Ratio) null results from its dark matter (WIMP) searches [68, 100].

For g -values, NEST is not an overfit to the LUX data. It includes results from global experiments produced over many decades, derived from taking S1 and S2 and solving Equation (18) for N_{ph} and N_{e^-} , or L_y and Q_y . The greatest deviations appear for g_2 , which had the greatest uncertainty. This was caused by the LUX extraction field being below what was necessary to extract close to 100% of drifting e^- s. While a g_1 is a probability in a binomial distribution, g_2 is more intricate, with the steps of S2 generation from drift to PMTs needing separate probability distributions to simulate S2 widths well [22, 108, 109].

A. Analytic Fits: Gaussian and Skew-Gaussian

In this study, we demonstrate that skew-Gaussian fits, accounting for skewness caused by α_r , provide a more accurate representation of data in liquid xenon dark matter experiments, outperforming traditional Gaussian fits by consistently producing lower χ^2 per degree of freedom and effectively capturing inherent asymmetries. The data are usually binned as in Figure 6. Centroids and widths are reported for each slice in (c)S1; widths are not errors, typically small for high-statistic data, but spread. Skew-Gauss fits capture non-Gaussianity. In III A and B, when we say skew, we mean $\log(S2)$ or $\log(S2/S1)$ skew, caused directly by α_r (defined by Eqn. 14 in [57], and not to be confused with α_p) and fits capturing that with a skewness parameter. Skew leakage will refer to the leakages calculated using such fits. Possible first-principles origins of skewness at multiple levels are discussed in [23, 28, 57].

The skew fits outperform Gaussian ones (Figure 7c). The number of degrees of freedom (or, the DoF) is comparable between the non-skew and skew fits, with 30 bins in y still, but only one new free parameter (DoF = 26 \rightarrow 25). With the exception of the first couple bins from NR, reduced χ^2 s also hover near 1.0, both above and below it, in spite of the increase in the number of free parameters. A fourth, skewness, is added to the three for a Gaussian (amplitude, center, sigma). Asymmetries are clear in the rightmost plot, which shows sample S1 slices. (Note low- E NR has features still not fit well.) The skew fits re-use the functional form of Equation (9)'s third line.

Overall reduced χ^2 s are 0.4 (ER band mean), 0.6 (ER width), 1.2 (NR band mean), and 1.1 (width) for binned skew-Gaussian fits, using LUX-reported errors. The χ^2 s over DoF are, respectively $-38/95$, $57/95$, $115/96$, and $106/96$ (p-values ~ 1 , ~ 1 , 0.09, 0.22). There are two free parameters in the DoF, the g s, with the linear noise levels set to 0% for S1s and S2s. The goodness-of-fit values come from direct comparison with no smoothing to band means or upper/lower uncertainties as done in Figs. 7a,b. (They use an empirical hyperbolic plus linear function explained in the caption.) On average the band means and widths alike differ by $< \pm 1\%$ for both ER and NR. The ranges for which these averages as well as both the χ^2 s are defined are S1=2-99 spikes for ER but 1.7-110.6 for NR. The minima are set by the 2-fold PMT coincidence level, and maxima by the decrease in statistics given the spectral shapes (significantly more events at low E_s).

“Spikes” refer to approximately-digital counting of individual photons detected, explained in [100, 111, 112]. Bin widths are 1.0 spikes for ER but 1.1 for NR, where bin centers are not integer values. D-D events were not isotropic in the detector, thus affected differently by po-

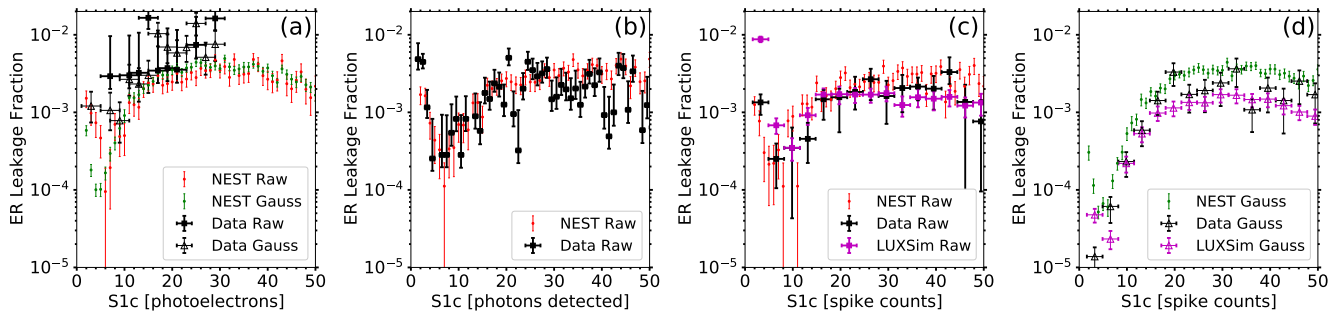


FIG. 8. LUX Run03 tritium and D-D calibration source runs combined to determine ER leakage past the NR band’s approximate center line, at 180 V/cm. (a) The first LUX publication [89], which used the traditional units for S1, phe a.k.a. PE. Raw leakage refers to counting the number of ER events which fall below the center of the NR band. Extrapolation via Gaussian integration is another option, as defined in Section I. (b) Later version of the same analysis using the higher-stat tritium run [30] where the S1 max was also increased, from 30 to 50. ER yields and backgrounds were better understood out to higher E s. The units were also updated to phd, with (re-)discovery of the 2-phe effect [76]. (c) S1 spike counting, improving upon phd [100, 109]. LUXSim included NEST but also more detail [110]. (d) The same plot as (c) from the same source but showing Gaussian-defined leakage.

sition corrections [113]. For every S1(c) bin (x axis), the default NEST binning was used along y, of $\log(S2/S1) = 0.6-3.6$ in 30 bins, to cover the extremities out to several sigma. All other settings were defaults for the LUX Run03 detector in NEST.

B. Analysis of the Energy Dependence via S1

In this section we begin the in-depth quantification of the fraction of ER events leaking into the NR region in the (default) $\log(S2/S1)$ vs. S1 space (Figures 6-7) with E dependence, via S1, at one field; the shape is qualitatively similar for all \mathcal{E} [18, 57]. S1 ranges and units are explored. Figures 7-8 indicate that leakage can be poorer (higher) at the lowest S1s, decreases at $\sim 5-10$, increases at 10-20, then flattens. (Later on, we examine how it drops rapidly above $S1=50$.) These features are driven by variations in the ER and NR band centroids and widths. Low leakage at relatively low S1s, combined with the default WIMP model having an exponential increase in signal at low E s due to the recoil kinematics, make LXe a great medium in the dark matter search. Even though E , and position, resolutions get poorer as E goes to 0, driving the widths of bands higher, the increase in the charge-to-light ratio from ER exceeds NR’s. If as was done on LUX, however, the PMT coincidence level is lowered (from 3-fold to 2), evidence emerges of leakage degrading again (Figure 8), due to width expansion becoming dominant. Low E leads to low statistics in N_{ph} and N_{e^-} , thus low pulse areas in S1 and S2, with large relative fluctuations in them.

While a PLR, used in many experimental results now, should account for the overlap of ER with NR in a continuous fashion, as with machine learning techniques [114], a specific and discrete value for the leakage or discrimination is easy to understand and more transparent. It provides rapid comparisons of experimental setups or analysis techniques and enables simple re-analyses of results.

Figure 8 shows leakage vs. S1. In the first plot, one can see that a standalone MC like NEST, non-detector-PMT-specific, tends to underestimate the leakage, either raw or

Gaussian. The cause is NEST not addressing variation in the 2-phe (photoelectron) effect per PMT. In the lowest bins the raw leakage was often 0, leading to empty data bins. Though improvement in leakage through XYZ corrections has already been explicitly demonstrated [115], a phd (photons detected) vs. phe comparison is missing, except across figures from different publications [89, 100]. Figs. 8a,b fill the gap. NEST slightly overestimates leakage between 30-50, but underestimates it in the first few bins, as it is not a full optical MC like Geant4 [116, 117].

In 8c, NEST matches well even at low S1s due to spike counting, which removes multiple levels of PMT-specific effects in analysis. LUXSim, based on NEST v1, overestimates leakage. In 8d, still using spikes, Gaussians overestimate leakage at high E but at low E underestimate it. The latter issue led to the phrase “anomalous leakage” [11]. NEST Gaussian leakage does not match data’s Gaussian leakage, but as stated earlier Gaussians are not good fits. Raw (non-analytic) leakage observed is more important but analytic approximations are still valuable due to the lack of infinite statistics in real data. Raw leakage must be modeled as closely as possible, to not overestimate or underestimate backgrounds. When detector-specific effects are not stripped away based upon data, a detector-specific MC like LUXSim is a better match, due not only to optical simulation of each PMT, but proprietary spike-count code (used for real data and MC).

While S1 dependence is a good place to start studying leakage given the possible E spectra of potential signals, a single number over an S1 range has utility. It not only allows for simple comparisons between experiments, but, more importantly, a simpler way to look at another dimension, \mathcal{E} dependence. It also makes it easier to see the non-negligible improvement achieved in moving from S1 as pulse area in photoelectrons to spike counting – that technique lowers σ_{ER} [30, 52, 89, 100]. σ_{NR} declines as well, but σ_{ER} is more important for leakage, if μ_{NR} stays \sim fixed (see Figure 7 left two plots). This is an analysis improvement requiring no alteration in the physical char-

| S1c Range | S1c Units | Raw Leakage $\times 10^{-3}$ | Gaussian Leakage $\times 10^{-3}$ | Skew Leakage $\times 10^{-3}$ |
|-----------|-----------|---------------------------------|--------------------------------------|----------------------------------|
| 1.5–30 | phe, PE | 1.69 ± 0.19 | 2.24 ± 0.16 | 1.35 ± 0.05 |
| 1.5–30 | phd | 1.74 ± 0.16 | 2.49 ± 0.71 | 1.44 ± 0.26 |
| 1.5–30 | spikes | 1.65 ± 0.16 | 2.28 ± 0.62 | 1.35 ± 0.25 |
| 1.5–50 | phe, PE | 2.48 ± 0.22 | 3.24 ± 0.76 | 2.00 ± 0.30 |
| 1.5–50 | phd | 2.51 ± 0.30 | 3.31 ± 0.89 | 2.03 ± 0.37 |
| 1.5–50 | spikes | 2.16 ± 0.24 | 3.04 ± 0.86 | 1.77 ± 0.33 |
| 1.5–100 | phe, PE | 2.24 ± 0.16 | 2.94 ± 0.66 | 1.78 ± 0.22 |
| 1.5–100 | phd | 2.04 ± 0.04 | 2.68 ± 0.42 | 1.67 ± 0.13 |
| 1.5–100 | spikes | 1.69 ± 0.08 | 2.35 ± 0.35 | 1.40 ± 0.11 |

TABLE I. Mean leakage across different ranges for S1_c (1.5–30, 50, 100) and units for S1_c: photoelectrons, phd, spikes, all compared directly with each other for the first time here. Typical NEST errors (systematics from seed choice and binning/fitting algorithms) on leakages are 0.3×10^{-3} , or, 15% relative. The intermediate stage of phd shows worse leakage than phe due to LUX’s detector specifics not being fully modeled. Note that for max>100 mean leakage is more stable, due to leakage falling by orders of magnitude out there (Fig. 9).

acteristics of a detector, such as higher g_1 and/or \mathcal{E} .

Skew fits come into play again as another software improvement. Table I compares raw, Gauss, and skew leakage, in different S1 ranges. Skew is closer to true leakage (raw *i.e.* counted) measured by counting but has the advantage of functioning when statistics become inadequate for a direct measurement, especially as S1 increases, and spectra of calibrations employed exhibit fall-offs [30, 67]. Skew modeling is applied in NEST not only as fits to individual S1 slices of the ER (and NR) S2 band in data, but directly in recombination: α_r leads to S2 skew.

Skewness modeling and fitting capture both the low- E increase in leakage beyond the naïve Gaussian assumption and high- E decreases in leakage compared to Gaussian fits. Asymmetry in the ER band results in fewer NR-like events. This is beneficial to a WIMP search, as first seen by ZEPLIN at high \mathcal{E} [118]. LUX later re-discovered it at much lower \mathcal{E} [57, 68]. Skew has been proposed as one way to explain XENON1T’s ER tail parameter [119].

The leakage derived by averaging over S1 from 2 to 50 spikes is 0.0018, within 1σ of data, even when considering only statistical errors. The final LUX Run03 analysis concluded $0.0019 \pm 0.0002(\text{stat}) \pm 0.001(\text{syst})$ [109] (99.81% discrimination). The large systematic error was driven by g_2 , which should be the same for ER or NR as a detector property, but it may have varied between calibrations. Recall that NEST assigns $g_2=12.2$ for NR but 12.9 for ER (11.5 and 12.1 in data, each $\sim 7.5\%$ uncertain). In switching to skew fits, the raw leakage switches from being 35% overestimated to $\sim 20\%$ underestimated *cf.* data. These appear to be similar problems, but as we

will see next, skew fits remain the best choice overall.

Raw and skew leakages are self-consistent within NEST and data (Figure 9). NEST overestimates leakage at high S1. Figure 6e hints this is due to NEST’s NR band being high. As L'_y and Q'_y alike match LUX data, this is likely due to the D-D neutron (n) E spectrum and final Xe recoil spectrum not being simulated well via NEST alone. Modeling of these necessitates transport through a complicated geometry [67, 105, 113]. The ER E spectrum is also not a match: a very non-flat (^3H) β spectrum [30] is the default in NEST thus far not the flattened one taken from [57] for Fig. 9, causing a 15–30% increase in leakage. E spectrum is a systematic for leakage (Section III D).

So far, what is most important is that NEST does not systematically under-/over-estimate leakage. This is critical for justifying NEST’s usage in our final conclusions later. Moreover, in Figure 9, despite NEST’s overestimation of leakage in that particular instantiation, we observe that 0.004 is the worst (highest) value (or, 99.6% discrimination), still superior to the original 0.005 benchmark coming from bad rounding of XENON10’s leakage [37].

C. Changing the Discriminant

Sec. C compares mean leakage for different 2D spaces and histogram settings, for ^3H and D-D. *Discriminant* is a pair of TPC outputs used to define leakage, the level of which can motivate the choice – historically $\log(S2/S1)$ vs. S1, but $\mu(S1) = \log(S2)$ is now more common, for fully separating S2 from S1. The band shapes are also simpler (Figure 10 top), as S1 and S2 both increase with the E . Leakage using $\log(S2)$ is equivalent: for S1s of up to 100 spikes, mean leakage (NEST) is 0.0016 (see the first entry in the last row of Table I). An analytic result with skew fits is also a good match, 0.0014 (last row, third entry). Using Gaussian fits instead again yields an overestimate: 0.00240, similar to the 0.00235 using $\log(S2/S1)$. That is only a mean: Figure 10 bottom shows underestimation at low S1s. This is most concerning if that is where most signals may lie. Mean leakages are similar across S1 ranges for different discriminants; we focus on S1<100, due to greater interest in higher E s stemming from EFT [120].

$\log(S2/S1)$ v. S2 [121] exhibits a leakage of 0.0043 (raw) in LUX Run03. Rejecting S2 in place of S1 as x, another option is E [15]. Combining S1 and S2 has been seen repeatedly to be superior to S1-only E resolution (in some cases S2-only) for ER or NR [23, 25, 56] but that is irrelevant to leakage. Raw leakage for our LUX standard does not improve: 0.0028 (*cf.* 0.002 on LUX, vs. S1 [100]).

For consistency and maximum backwards compatibility of NEST comparisons to the greatest number of older works, we continue with $\log(S2/S1)$ as the y axis (S1 as x) for the remainder of this work. Based on this section, our conclusions should be generalizable to $\log(S2)$ as y.

Our common x-axis range for each comparison will be S1 of 2 to 100 spikes (similar to phd) in NEST for LUX’s initial WIMP search: 0.0016 raw leakage (or 0.0019 if defined without binning, counting as leakage any ER event with S1<100 falling below a continuous fit to the mid-

dle of the NR band) and 0.0015 for skew (*i.e.*, a 99.84–85% discrimination). One built-in feature of NEST is the ability to consider the NR band raw means, medians, or skew/Gaussian-fit centroids (which are not the peak or mode in skew fits) with or without a continuous fit across $S1$ bins. This systematic creates a difference far smaller than the 15% error in Table I (see Figure 10 top).

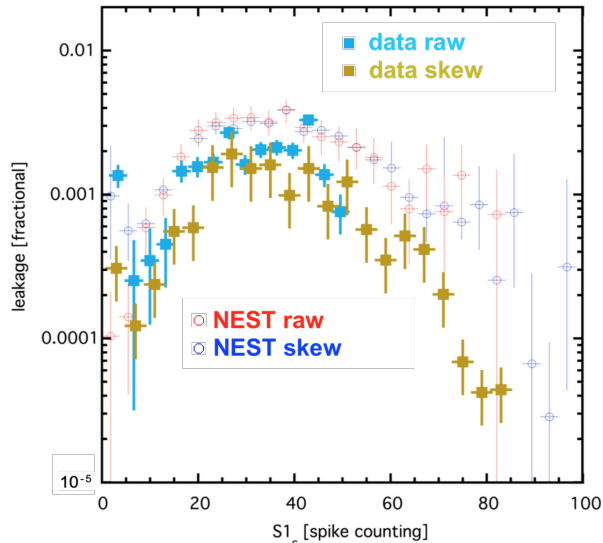


FIG. 9. Leakage in different techniques: raw [109], skew [57]. Offset histogram bin centers and widths are shown for clarity: the latter are 3.35 spikes (cyan squares, identical to Figure 8, second from right), 4.0 (gold squares), and 3.65 to be in between. NEST $S1_c$ spans 0 to 98.5 in 27 bins. Red circles are repeated from Figure 8 second from right, but with this different binning, which affects the first few bins the most, thus underscoring the importance of sensible histogram settings when characterizing leakage. NEST’s blue circles (skew) match the actual leakage in cyan in the first bin, despite being an analytic approach. They match better than gold, which differs in binning but is the same (actual) data as cyan (light blue).

D. Changing the Underlying Energy Spectra

This section delves into the role of calibration source E spectra in influencing leakage, explains how using NEST agreement allows extrapolation to sources not deployed by LUX, and illustrates how this understanding of leakage can aid in estimating its impact on WIMP detection, emphasizing LXe’s suitability as a low-mass dark matter target. Contradictory results on leakages from nominally similar experiments may be created by differences in the spectra. For example, for a similar range of $S1$, Dahl [15] found ~ 0.004 at 4,060 V/cm, while ZEPLIN-III FSR at 3.85 kV/cm reported 0.0002 [123]. This suggests leakage is even less universal, depending not only upon E range and binning and g_1 , but also on sources, and the nature of backgrounds. For ER, interaction type differs (β , γ).

LUX Run03 only had a ^3H ER calibration (^{14}C later), with D-D the main NR calibration, but after establishing NEST agreement with data we extrapolate to non-LUX sources, instead of comparing to experiments that used

other sources but had different g_1 , g_2 , \mathcal{E} , etc., introducing systematics. Table II reports raw and skew leakage for 5 ER and 5 NR sources. $>10\times$ leakage changes are seen.

Regardless of what underlying E spectra are assumed, the calculated leakage based on them never exceeds 0.005 in the table. D-D may lead to conservatively overestimating leakage, compared to AmBe or Cf calibrations, as well as a 50 GeV WIMP. For the bottom half of Table II, the simplification of one single g_2 definition occurs, assuming ER and NR must use the same value, and that the NEST

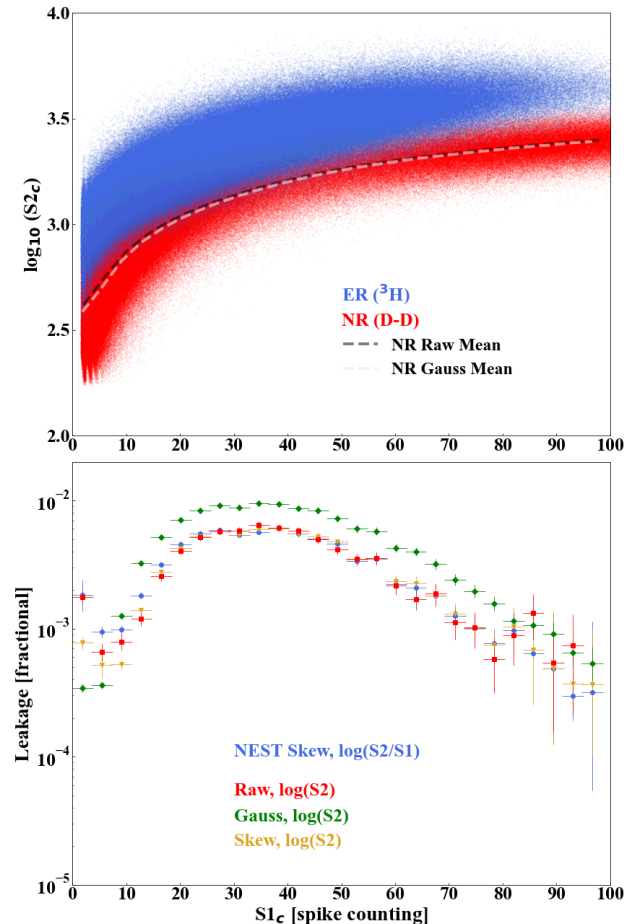


FIG. 10. Top: $\log(S2)$ as discriminant in LUX data, as simulated by NEST, for tritium in blue and D-D in red. Discrete points are shown, though the identical functional form from $\log(S2/S1)$, a hyperbola plus a line, would fit. This plot highlights different features: higher density in the middle for ER (β spectrum) but at the extremes for NR (D-D E spectrum). At low $S1$ s quantization is evident (from the spike counting). Dashed lines indicate the difference between a line of NR averages and Gaussian centroids. Bottom: $\log(S2)$ leakage vs. $S1$, with NEST skew selected as the example from $\log(S2/S1)$ discrimination, repeated from Figure 9 in blue again. Red, green, and yellow are the three options for quantifying leakage, with blue, red, and yellow all consistent across $S1$ s. Green (Gaussians) is the outlier. $S2$ without a \log_{10} (XENON1T) was not explored as it requires the complication of a log-normal fit or logarithmic bins to work well, in a PLR [122].

yields are correct. The D-D run best-fit g_2 was lower than this unified (average) value, so this action conservatively raises the NR band, raising leakage slightly.

| Source | Raw Leakage | Skew Leakage |
|--------------------|------------------------|------------------------|
| <i>Tritium</i> | 0.0017 | 0.0014 |
| ^{14}C | 0.0010 | 0.0010 |
| ^{220}Rn | 0.0012 | 0.0013 |
| <i>Flat Beta</i> | 0.0013 | 0.0012 |
| <i>ER Mixture</i> | 0.0039 | 0.0035 |
| | | |
| <i>D-D neutron</i> | 0.0025 | 0.0025 |
| <i>AmBe</i> | 0.0019 | 0.0020 |
| ^{252}Cf | 0.0018 | 0.0018 |
| <i>50 GeV WIMP</i> | 0.0017 | 0.0017 |
| <i>Boron-8</i> | $\sim 3 \cdot 10^{-5}$ | $\sim 3 \cdot 10^{-5}$ |

TABLE II. Leakage changing with band shape changing due to E spectrum. All values are NEST’s, but vetted using LUX Run03. Top: NR E spectrum is fixed as D-D. The first four rows are different β spectra (^{220}Rn leads to ^{212}Pb [124]). Flat means constancy in E , more representative of a real ER background [28] and lower in leakage [57]. The fifth row is a mix of β or Compton-like interactions with x-ray or gamma-ray photoabsorption: leakage is increased, as Q_y is smaller for gammas [28, 44]. This should not be very applicable to next-gen experiments, where the Rn-chain naked β s and ν interactions will dominate the ER background [125]. This might however explain higher leakage in past ones [106]. Bottom: As a compromise, leakage for the case of a combination of flat beta ER (lowering it) with treatment of the worst-case scenario of the g_2 systematic in LUX (raising leakage more). Maintaining the identical g_2 for ER and NR, the NR sources are: D-D, earlier calibrations, then natural sources.

The E spectrum effect is quantified for WIMPs in Figure 11. Leakage drops significantly for low-mass WIMPs; thus, Xe is a good target for them, despite its high mass number, even without considering S2-only analyses [126]. ^8B ’s E spectrum is most like that of a 6 GeV WIMP [7]. After first matching a real NR band with NEST, the benefit of using CE ν NS and WIMPs is avoidance of detector geometry specifics, neutron scattering cross-section uncertainties, and multiple scattering.

E. WIMP NR Signal Acceptance

This section explains why a flat NR E spectrum is not WIMP-like, discusses how $>99.9\%$ discrimination is possible with lowered NR acceptance, and mentions some experimental challenges. So far we have used the NR band centroid with linearly or smoothly interpolated (skewed-) Gauss-fit means (between S1 bins). This implies 50% NR signal acceptance, assumed for years [37, 106] even with the advent of PLR (Profile Likelihood Ratio) [89]. But it is slightly less due to means and medians differing, and fit values compared to raw values. The NR band has a positive skew overall like the ER band, for multiple reasons, like recombination and quenching. Resulting reduction in acceptance is only a few percent, and the opposite effect, more acceptance from negative skew, may occur at

low S1, for different spectra [57, 67, 106].

The leakage for the NR band from the flat- E spectrum under LUX conditions plus a flattened- E β spectrum is 0.00319 raw (0.0032 skew) for a $48.7 \pm 0.3\%$ acceptance ($S1_c$ of 0 to 100 spikes). This exceeds the leakage for even a 100 TeV WIMP, the highest mass tested for Figure 11, with leakage at that high of a mass still only 0.0024 (raw and skew alike). A flat NR band is thus a poor fit even for an ultra-heavy WIMP. Using it is conservative.

Figure 12 plot has different lines for flat- E NR signal acceptance from 5-99% (bottom-top, red-violet), post triggering efficiency. These are still estimates, assuming that Gaussians describe the band slices. Non-Gaussianity may cause a few percent deviation in each bin. The red points, which should be viewed from the right y-axis, break down raw (counting) acceptance by S1 bin, for the black line, which has an overall acceptance in this range of nearly 50% (actual 49%). The low level in the first bin is due to S1 and S2 thresholds removing events from the band.

The middle pane shows leakage as a function of different signal acceptances from the rainbow in the top plot. It demonstrates that even 99.9+% discrimination is possible with reasonable acceptances, of 20-30%. 99.5% discrimination occurs slightly above 50% acceptance.

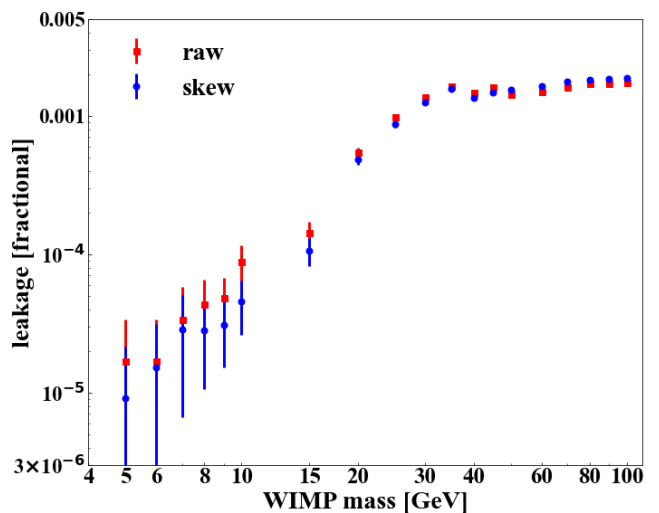


FIG. 11. ER leakage (flat- E background spectrum) as a function of WIMP mass in GeV/c^2 from both counting (red) and skew fits (blue) for LUX Run03 conditions [100]. The former (raw) becomes difficult to quantify, possible only through very long simulation runs (due to the higher statistics required) as mass approaches 0. Leakage asymptotes to a maximum possible value as mass goes to infinity. For clarity, the plot stops at 100 GeV, but masses up to 100 TeV were explored, and the leakage asymptotes to 0.0024 (a 99.77% discrimination), still better than 0.005 (99.50%), despite 180 not being the optimal field for leakage, closer to 300 V/cm [57]. The lower low-mass results, clustered at lower S1s where it was shown leakage rises for a fixed NR band, are due to the NR band centroid moving down in S2, away from ER, as shown in Fig. 7 of [127] for ^8B .

At bottom is acceptance vs. keV in red (bottom x) and mass in GeV in blue (top x) for the case of a traditional, flat band. Not only does the leakage decrease as WIMP mass approaches 0, due to the lower-energy E spectrum, but the acceptance does not correspond with that calculated from a uniform E spectrum. The actual center lines for these lower- E spectra move down in $\log(S2/S1)$ away from the ER band. A PLR handles all this internally but these effects are rarely noticed as a result of the “black box” nature of that statistical tool [14, 109].

To capitalize on those effects, experiments will need to address single/few- e^- and photon backgrounds leading to accidentals coincidences, and other effects such as PMT dark noise within detectors with hundreds of PMTs [128]. S1 and S2 thresholds will need to be lowered, especially from 3-fold S1 to 2-fold S1. Recently, this coincidence requirement has instead been increased, due to the larger numbers of PMTs in use, from 2-fold to 3-fold S1. That avoids random noise leading to false-positive S1 signals being reconstructed from individual photo-electrons in a few PMTs [129, 130]. Nevertheless, even for 20 GeV the fraction of WIMP events below a flat NR band mean is already $>60\%$, rising steeply as WIMP mass falls, to 90% at 5.5 GeV (consistent with ^8B). A PLR will essentially combine enhanced acceptance with lower leakage, by setting an effective acceptance corresponding with an expected leakage of <1 background count.

F. Switching from LUX to XENON10; Higher S1s

This section explores the limitations of a LUX focus, by scrutinizing XENON10’s leakage, and of the “vanilla” WIMP model, by considering higher energy. While LUX Run03 is relevant to LZ’s first science run given its comparable conditions [133], XENON10 [37] had a lower g_1 , but higher g_2 and fields than LUX, broadening our scope to other possible detector conditions. While it is unlikely future projects will achieve similar fields, a non-LUX S1 dependence is a good second comparison.

In Figure 13 at left, we review distinct interpretations of the same data: changing S1 ranges and bins, and fit algorithms [37, 131, 132]. Official leakage values are red circles. The middle plot compares NEST with select examples from the left one, with the greatest S1 ranges. As seen earlier, Gaussian fits tend to overestimate leakage. Raw leakage seems to be underestimated, especially near 10 phe (15 keV_{nr}) but otherwise NEST agrees with data.

The x-axis terminates as high as possible at the right for XENON10, $S1_c = 165$ phe, still not as high as possible in E , as the NR calibration at the time was AmBe, with an endpoint of 330 keV_{nr}. Our plot now ends barely above 100 keV in S1-reconstructed NR E but it has the highest-S1 data made public. No skew fits and/or skew-extrapolated leakages are available from XENON10. We rely on Gaussian extrapolation for the majority of bins, above 50-60 keV_{nr}, where raw leakage in data was zero. NEST agrees well (the blue squares compared to black dashes) concurring on $< 10^{-5}$ leakage above 100 keV_{nr}.

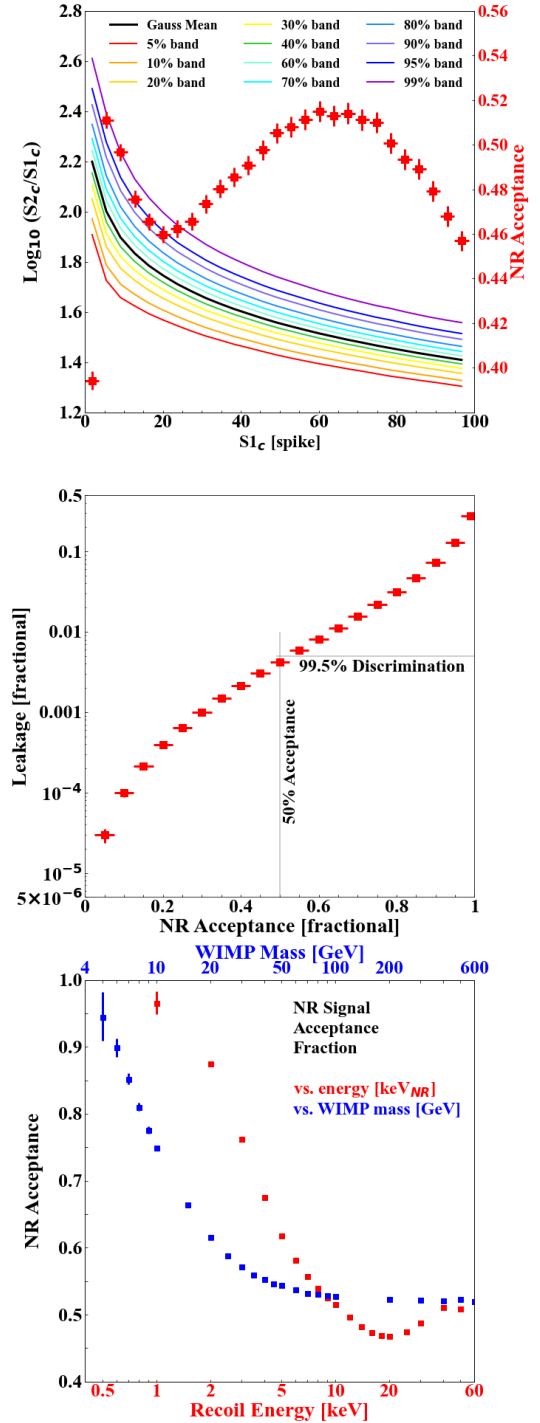


FIG. 12. Top: A color scale of different possible NR band lines of a constant- E spectrum, with 5-99% acceptance underneath. The black line indicates Gaussian means (not medians). The black line is nominally the 50% dividing line. The breakdown of acceptance for S1 bins is in red, exhibiting undulations due to the NR skew changing with E , and averaging to only 49%. Middle: Leakage tied to varying flat signal acceptances at top. Bottom: Signal acceptance as a function of truth E (not S1) in red, using smeared NR events of only those E s, and versus WIMP mass in blue, each representing a falling- E spectrum. All values are for below the black Gaussian-fit mean, flat-NR line, thus varying in leakage (but always less than 0.005).

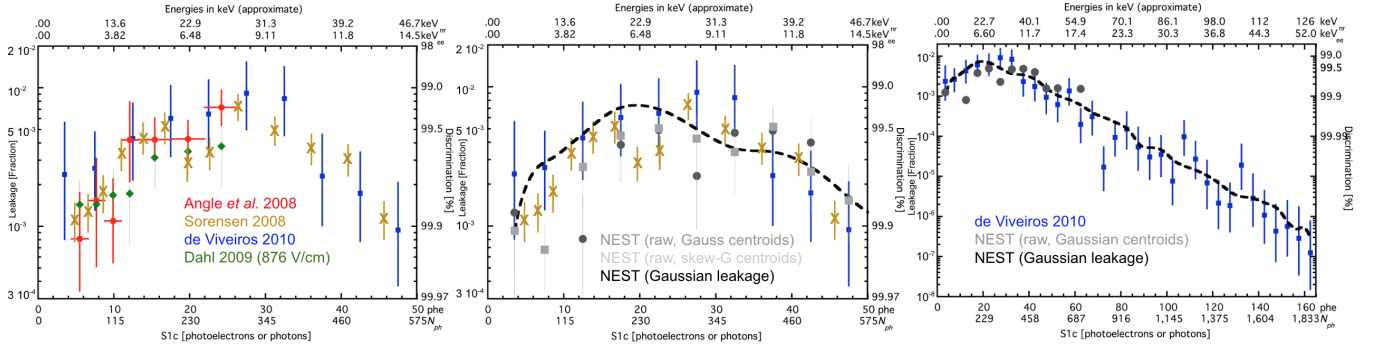


FIG. 13. Left: Different leakage interpretations in the same data: XENON10, 730 V/cm. Red circles [106] and yellow Xs [131] are raw, while blue squares [132] and green diamonds [15] are from Gaussian fits, with the latter in another detector (Xed) at a similar field, 876 V/cm. For clarity, x errors, which indicate bin widths, are included only for red, but bin centers/sizes are similar for all points. Only blue and yellow extend beyond XENON10’s search window. Bottom x-axes indicate both raw numbers of photoelectrons (XYZ-corrected) as well as a conversion into photons reconstructed using XENON10’s $g_1 = 0.075$ [15, 37, 131]. Top axes are approximate central E s for each bin for ER and NR, on an S1-based E scale. Middle: The same yellow and blue points are repeated from the left, omitting others for clarity, while adding the NEST comparisons. Dark gray circles and lighter gray squares are raw leakage in different random instantiations of a simulated XENON10 detector with ER and NR calibration statistics comparable to those in the real experiment. In addition, the darker gray circles use Gaussian fits to determine the NR band centroid, while the light gray squares use skew-Gaussian fits, still using means as a band centroid. They show raw leakages by counting, not extrapolated utilizing the skew functions. In dashed black is a smooth eye-guiding (not a fit) line of Gaussian leakages by bin. Right: The same blue squares and gray circles (errors omitted for clarity) and black dashes from the middle, but extended to high E s. Here NEST is compared to the only available data this high in S1 and E , from a PhD thesis [132].

In a typical SI WIMP search, a LXe TPC cannot capitalize on this, as even large-mass WIMPs produce negligible signal at this high E . However, if one entertains certain EFT operators [120], not only is some signal still possible (as high as 500 keV_{nr}), but because of peaks in Bessel-function form factors some operators predict the majority of WIMP signal could occur at hundreds of keV for NR [2, 122]. This has motivated new calibrations [134].

Given the lower g_1 and higher \mathcal{E} , which we will see in the next section is also conservative, the leakages in Figure 13 (right) are not the best possible, yet LAr-like (S1 PSD) leakage [135] is estimated to be achievable, 10^{-9} , at $S1_c = 250 \text{ phd}$, by extrapolating Figure 13, although for $\approx 50\%$ NR acceptance. PICO-like leakage [136] of 10^{-10} seems possible above $S1_c = 300 \text{ phd}$, still only $\sim 50 \text{ keV}_{ee}$ on average for LUX detector conditions (not XENON10), corresponding with only 160 keV_{nr} [68]. With increasing E and S1 (and S2), the ER and NR bands continue to diverge, with ER bands not expanding significantly enough in σ_{ER} to prevent ER leakage from continuing to decrease (significantly). ^{14}C band data continued in LUX Run04 to its beta endpoint of 156 keV_{ee} at S1s of over 600 phd and corresponding NR energy of 288 keV [17]. In experiments such as LZ [133] and XENONnT [124, 137] ^{220}Rn will serve the same high- E calibration purpose.

There are two important caveats on the benefit of low leakage at higher E s. One is the γ -X *i.e.* MSS (multiple-scatter, single-ionization) background. It needs to be better understood, via MC, a cut or background subtraction, or a combination. It is doable [122, 138]. The second is gamma photo-absorption peaks exhibiting higher leakage than β s and Compton scatters, due to lower S2s [28].

G. Electric Field and g Dependencies

This section brings together our XENON10 plus LUX Run03 examples, while adding comparisons to Run04 and many other detectors and runs, to elucidate the influence of \mathcal{E} , g_1 , and g_2 (includes the GXe extraction field) all together on the discrimination performance, as continuous variables. A local minimum in leakage for a drift E-field of approximately 300 V/cm is seen. For simplicity, S1 dependence is replaced with individual leakages, means over representative $S1_c$ ranges. XENON had poorer discrimination on average than LUX Run03/04 and other later experiments, despite running at a significantly higher \mathcal{E} , easier to achieve earlier with lower cathode HV inside of a smaller TPC. In its WIMP search space ($S1_c < 25 \text{ phe}$), the value was 99.6% on average (a 0.004 leakage) and it did drop below 99.5% discrimination (>0.005 leakage) in some $S1_c$ bins (again, Fig. 13). Parts of the explanation are bigger σ_{ER} from lower g_1 , and phe as the S1 units, not phd. (The 2-phe effect was unknown during XENON10.)

Higher \mathcal{E} allegedly improves leakage [143], but thanks to a fuller modeling of the NR and ER band means and ER band widths, there now exists a more complete answer [57]. Drift fields above $O(1) \text{ kV/cm}$ will increase the σ_{ER} , but also $(\mu_{ER} - \mu_{NR})$. At electric fields $O(100-500) \text{ V/cm}$, there exist undulations in leakage, as $\mu_{ER}(S1_c)$, $\mu_{NR}(S1_c)$, $\sigma_{ER}(S1_c)$, plus ER band skewness (based on α_r) all change at different rates. So, we have an answer for the origin of the 0.005 leakage (99.5% discrimination) benchmark for LXe TPCs (historical and mainly hearsay now, but see [128] and ref. therein, especially [37, 106]). The high \mathcal{E} at which XENON10 ran placed it near a local

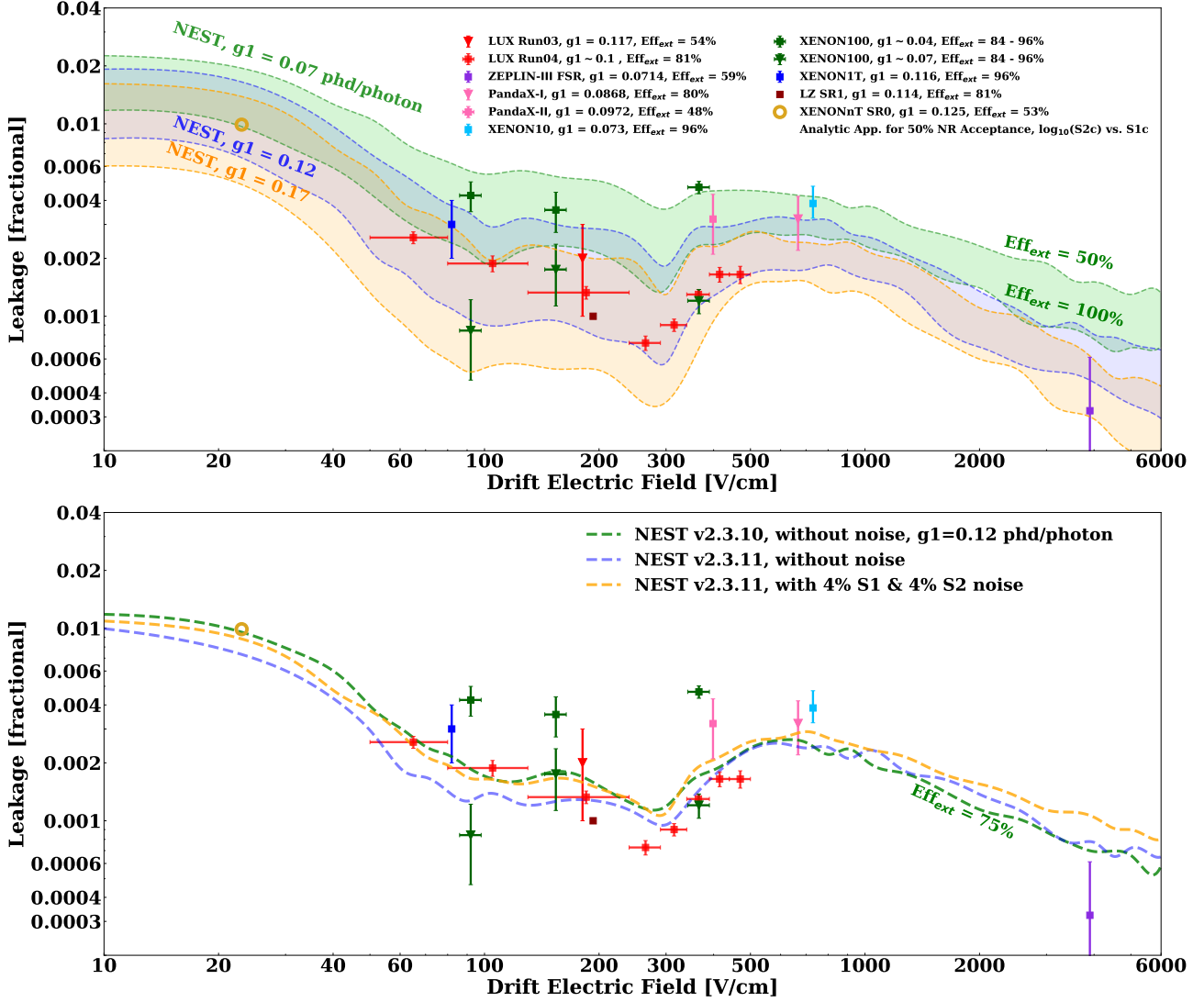


FIG. 14. Top: All known (raw and skew) ER leakages [18, 35, 37, 57, 109, 118, 133, 139–141], for centrally-defined NR bands in $\log(S_2/S_1)$ vs. S_1 (colored points with errors) with three NEST examples (skew) as colored regions (not fits: eye guides). In the legend, acronyms FSR / SR0 / SR1 refer to a first science run. The XENON100 g_1 values were 0.05 and 0.08 PE/photon, where PE is the same as phe (PMT photoelectrons). LZ has no error reported [133]. XENON100 was able to explore different g_1 via detector slices from different positions. Each NEST bands spans 50-100% extraction. The central one uses LUX/LZ/1T-like g_1 . The middle of this band should be compared to LUX Run04, with data for the most fields. Data exist for fields not reporting leakage directly, with means and widths still informing NEST between 0-4,000 V/cm. LUX Run03's lower extraction ($\sim 50\%$) likely causes higher leakage at 180 V/cm, though the (systematic from g_2) error is too large to conclude that. The lowest NEST band is an estimated best possible with current technology, for a moderate-mass WIMP and 50% NR acceptance, combining an LZ-like g_2 [133] with a high g_1 , less than the best achieved [142]. The upper (light green) band is close to the lower g_1 value of XENON10, converted into phd/photon. XENON100, which studied $g_1 = 0.07$ plus 0.04, used different E spectra and S_1 ranges than the defaults here, so agreement with it is only partial. Bottom: Comparison of NEST version used throughout this work (2.3.10) with the latest one (2.3.11) with ER (and NR) resolution parameters reduced by 10% (and 60) to account for LZ and XENONnT data. Noise is added to raise v2.3.11 in leakage to address older detectors' specifics. This suggests earlier iterations of NEST overestimated intrinsic fluctuations, inadvertently absorbing detector effects, and making this paper conservative.

max in leakage: Figure 14. With significantly more data, and a better understanding of microphysics, we see the best \mathcal{E} seems to be ~ 300 V/cm as an emergent property.

Within uncertainties, there does appear to be a flat region between ~ 80 -390 V/cm, with contradictory data between XENON100 and LUX Run04, and NEST splitting

the difference: Figure 14. This compromise approach for NEST is not forced, as NEST does not, and cannot, (be) fit directly to leakages. Its internal models are based on generating yields and E resolution which match the raw data of ER and NR band means, and widths, from all available calibration data sets, at different fields and g_1 .

Neither a PLR nor literal counting of ER background events falling below the NR-centroids curve should exhibit a substantive difference in the final results in this field range. PLR performs background subtraction, while the latter involves a simple, near-50% NR acceptance. Thus, other types of backgrounds may be of greater concern. Nevertheless, a target now exists of 300 V/cm for a next-generation LXe TPC to achieve. Figure 14 suggests that, coupled with a high enough g_1 and g_2 (within reach of current technologies), a similar order of magnitude of leakage and discrimination, $O(5 \times 10^{-4})$ and 99.95%, can be achieved at that much lower field as at 4 kV/cm.

Lowering NR acceptance, already done on XENON100 [36] and as projected for DARWIN [144], to *e.g.* 25%, has already been shown in Section E to decrease leakage, so even low fields can lead to competitive searches (limits or discoveries). Achieving a good balance between signal acceptance (NR) and background acceptance (ER leakage) is the same requirement as in any HEP experiment.

GXe field plays a role, too. g_1 and drift (liquid) E-field have the largest impacts, but a low extraction efficiency can widen the ER band just as low g_1 does. Thus g_1 , g_2 (product of single e^- S2 pulse area in phe or phd, and extraction), and \mathcal{E} are all considered together in Figure 14. Within the components of g_2 , the binomial extraction (a stochastic loss, not a fixed reduction) is more important than the precise Y_e for leakage. A single-phase TPC may resolve this, if it can work well at low, WIMP-search E s (keV scale) not just at the E s of $0\nu\beta\beta$ (MeV) [3, 145].

Earlier the key roles played by the NR and ER E spectra were already addressed, so to maintain simplicity in Figure 14 the NR spectrum was always D-D (based upon the LUX geometry) and the ER one was always flat beta. The latter is an excellent approximation of a full combination of all backgrounds for the WIMP-search-relevant E range in most detectors [28, 133], while the former is approximately like a 50 GeV/ c^2 WIMP [67] except with higher leakage (Table II).

As $S1_c$ range was shown to impact leakage as well, another (simplicity-motivated) choice was made. Figure 14 shows three S1 search windows. The central band has a LUX-like $g_1 = 0.12$ phd/photon and $S1_c$ max of 100 phd, while the min was determined by the 2-fold PMT coincidence. For the lower band the max $S1_c$ was extended out to 150 phd, corresponding with the improvement in g_1 . For a fixed $S1_c$ range, distinct g_1 s would not exhibit any significant difference in leakage, due to the E range corresponding with the window shifting. Lower- E events will fall below threshold as g_1 decreases, while new, higher- E ones come down into the S1 window. Events at E s with higher and lower probabilities of leakage cancel. For the upper band, $S1_c = 4.5$ –20.5 phe in 16 bins, for comparison to XENON10 data (note the change in units) which was also matched earlier, by individual $S1_c$ bin.

H. S1 Pulse Shape Discrimination (PSD)

Our discussion of Xe ER leakage would be incomplete without mentioning PSD. Like LAr's, LXe S1 pulse shape

for NR is more prompt compared with ER: dimer singlet states are more likely than triplets. This is due to higher NR dE/dx , and singlets having a shorter decay t [147]. While PSD can be used in place of $\log(S2/S1)$, *e.g.*, in a zero-field, single-phase (non-TPC) detector like XMASS previously [148], or in addition [57, 100, 111], it is less effective in LXe. In LAr, the difference in time between the two states is far greater [135].

Pulse shapes were modeled in NEST [108], updated using LUX [111, 114], and checked against XENON [149]. Contradictory data exist on fundamental parameters like singlet/triplet ratio, and the question of a separate (non-zero) recombination time. There are degeneracies across many values, allowing NEST to match contradictory results with one model. *E.g.* an experiment may report no recombination time and more triplets, or higher recombination time and fewer triplets, to produce a similar time profile, even if unlike the singlet and triplet decay profiles the recombination one is non-exponential (t^{-2}) [150].

First-principles aspects of pulse shapes are difficult to model, due to photon travel times (especially in larger detectors) and additional time constants added by PMT internals, cables, pulse-shaping amplifiers, as well as other unique DAQ aspects. Nevertheless, some conclusions are possible from existing work: some degree of PSD exists, but is orders of magnitude lower than LAr's or the S2/S1 discrimination in LXe [147, 148]. But, the combination of S1 PSD with S2/S1 is powerful [57] under specific conditions. The E (and g_1) must be large enough to allow for sufficient photon statistics. This may preclude the vanilla WIMP, but work for a subset of EFT operators. \mathcal{E} must be low enough for PSD to work for a WIMP, by raising L_y and also making the S1 pulse shapes of ER and NR more distinct (given the changing physics as $\mathcal{E} \rightarrow 0$, as demonstrated by Fig. 2 in [108]).

ER and NR S1s become similar as $\mathcal{E} \rightarrow \infty$ in Xe [151]. The one at-scale PSD attempt (WIMP detector) was thus at null E-field [148]. Singlet/triplet ratio may drop with field [111, 149], and/or recombination time may vanish, with increasing \mathcal{E} . That is reasonable, as recombination is suppressed as S2 increases. As \mathcal{E} decreases, PSD begins to be usable, if combined with S2/S1, even at traditional WIMP-search E s. A combination leads to a leakage reduction of more than 2x, outside of error at <100 V/cm and $S1_c = 10$ –50 phd [57]. Mid-range S1 also corresponds to the highest S2/S1 leakages (Figure 8). At higher S1s, correlation between NR-like shape and NR-like S2/S1 for ER makes a combination less motivated.

Figure 15 demonstrates the present state of the art. New advances in photo-sensors enabling picosecond timing resolution [152], if they can be leveraged for G3, might make PSD more beneficial. But that is only true if coupled with a sufficiently large g_1 . The cylindrical geometry of a TPC (as opposed to spherical like XMASS) may still pose a challenge, due to complicated photon paths from multiple reflections, which reduce the initially ample information from single and triplet decay timing.

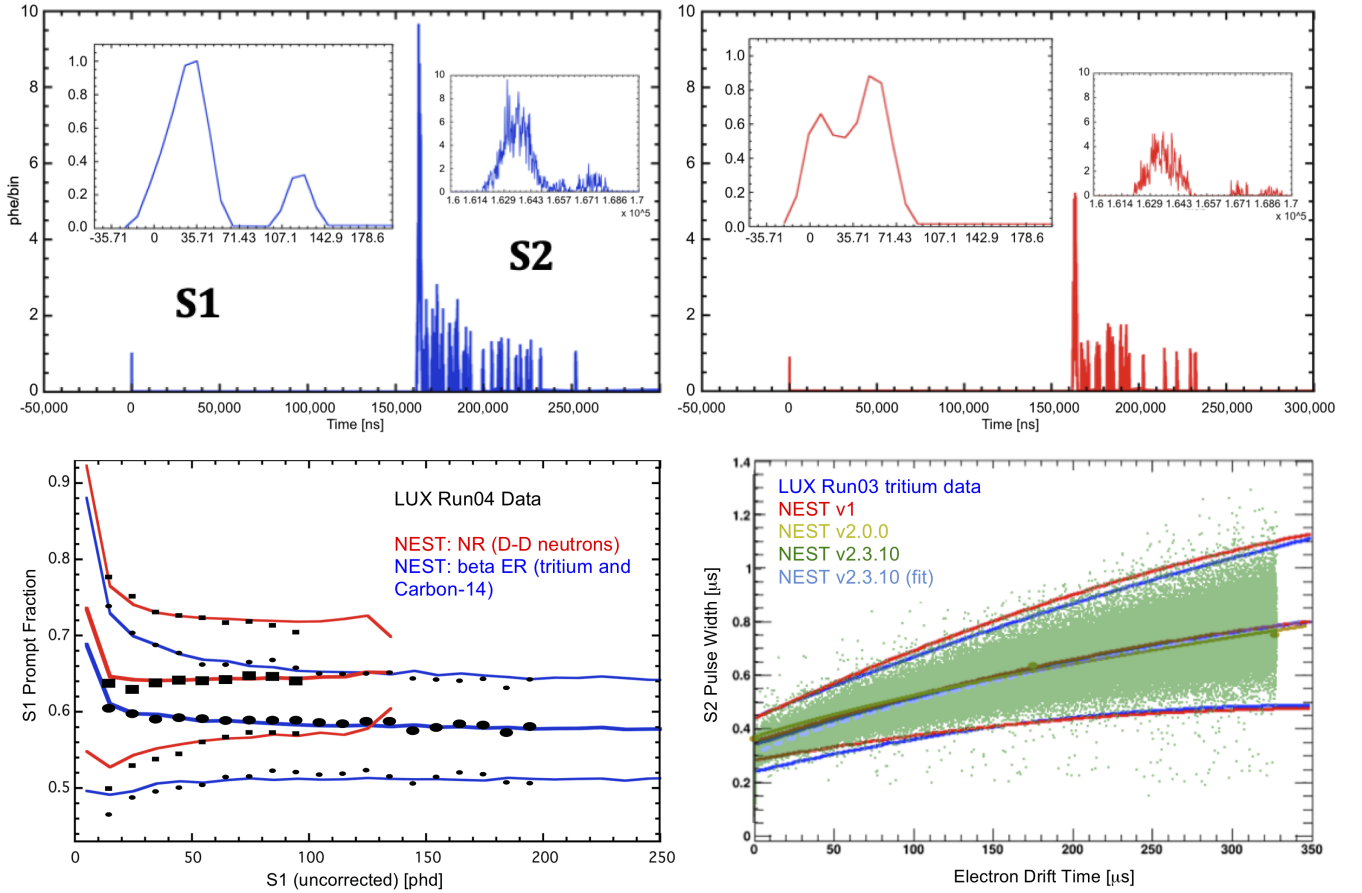


FIG. 15. Upper row: sample events demonstrating NEST’s S1 and S2 pulse shape simulation capabilities, with ER in blue (2 keV beta) at left and NR in red (8 keV) at right. While joined by straight lines to match historical depictions of LXe pulses, the individual points represent centers of 10 ns time bins (most experiments employ a 100 MHz digitization rate [129]). Modeling of an e^- train [146] of late-extracted e^- s is evident as S2 tails extending to the right. Bottom row, left: NEST’s consistency for S1 prompt fraction medians as well as medians \pm the standard deviations, with actual LUX data as circles (ER) and squares (NR) [111]. More NEST-data agreements for S1 prompt fraction as functions of S1 as well as \mathcal{E} are demonstrated in [114]. For precision quantification of PSD and its combination with $\log(S2/S1)$ discrimination, see Figs. 14–17 of [57]. Bottom row, right: Comparison of NEST with LUX tritium S2 width as a function of the drift time, a measure of the depth in the TPC. S2 pulse width is crucial for estimating z position for fiducial volumes cuts, when the traditional ER discrimination is lost in an S2-only analysis. Lines are means \pm standard deviations (widths in the width). NEST agreement for XENON10 can be found in [108].

IV. DISCUSSION

Beginning with models of beta ER, gamma-ray ER, and the NR light and charge yields, along with resolution modeling, a coherent picture was built up inside of the NEST framework, which enabled a good agreement with data. NEST was also shown to have features from multiple first-principles approaches such as the box and Birks models. Because light and charge become digitized S1 and S2 pulse areas, comparison of NEST to data on means and widths in S2 vs. S1 was performed, launching a leakage study using detector observables, with LUX’s Run03 at 180 V/cm as the example detector. LUX also had a very typical S1 photon detection efficiency, $g_1 = 0.117$ phd/photon.

ER backgrounds in the NR regime in S2 vs. S1 were studied as raw leakage or the leakage extrapolated from Gaussian or skew-Gaussian fitting. The analytical func-

tions are effective for extrapolation in low-statistic calibrations, but neither option is error-free, with Gaussians tending to overestimate leakage and skew-Gaussians underestimating it. The former scenario may be conservative for projecting detector performance, but can lead to artificially-low WIMP limits by an overestimation of expected background in a PLR. The latter (skewed) seems closer to true leakage. As S1 increases, all leakage calculation methods exhibit an increase then plateau, followed by a rapid decline as S1 goes to ∞ with increasing E_s .

Different units for S1 were also probed, starting from quantifying basic pulse area in photoelectrons but then switching to phd, a unit pioneered by ZEPLIN and LUX, followed by spike units. Pulse areas in phd are lower compared to areas in phe, caused by a stats-based compensation for the 2-phe effect, where 1 incoming (VUV) photon can produce multiple phe. Digital counting of individual photons (called spike counting) is a further improvement,

reducing leakage by reducing the ER width σ_{ER} .

While no significant difference was found between leakages from $\log(S2/S1)$ and $\log(S2)$, now the more common y axis, the latter has more skewness. This can lead to a general overestimate of leakage if skew fits are not done, depending on the S1 and the detector conditions. Skew-Gaussian fits perform well in NEST due to its underlying skew-recombination model adding skew to a binomial (or Gaussian, for high statistics) recombination model for N_{e-} . S2 and E were both worse than S1 as an x axis for leakage calculation.

The E spectra have major impacts on ER leakage as well as NR acceptance, and higher-mass WIMPs will produce higher- E spectra. A softer E spectrum leads to significantly less leakage: ^8B (ν) NR and low-mass WIMPs are farther from an ER band. To lower leakage further, NR acceptance can be reduced to find the optimum balance between acceptance of signal (NR), and the acceptance of background (ER).

The largest leakage, or lowest discrimination, occurred within the first LXe TPC experiment with world-leading dark-matter-search results (XENON10) primarily due to its high drift (liquid) field. Higher g_1 and g_2 , the S1 and S2 gains, with higher extraction efficiency (via a higher GXe field) can improve leakage. A higher liquid drift field does not monotonically lower the leakage. The best drift field for reducing leakage down to 5 parts in 10^4 seems to be ≈ 300 V/cm, but lower drift field (50-80 V/cm) may at least permit < 5 in 10^3 if coupled to S1-based PSD.

0.0005 is not directly measured close to 300 V/cm and would require a higher g_1 at least, but such a low leakage is plausible:

1. Higher g_1 is possible with new photon sensors [153] claiming quantum efficiencies as high as 100+% for VUV. Strong, monotonic dependence of leakage on g_1 is clearly demonstrated by Figs. 10–11 in [57].
2. Modeling the influence of higher g_1 on σ_{ER} is trivial in NEST (or any MC), as it just drives a binomial process. Our claim does not rely most upon skew or other, more-uncertain parameters ([28] established g_1 , g_2 , and \mathcal{E} as most critical to any detector modeling).
3. XENONnT and LZ's first results have forced a re-evaluation of Fano factors and recombination fluctuations for NR and ER, hinting that NEST v2.3.10 and earlier was overly conservative in leakage predictions, by accidentally absorbing detector effects no longer applicable to modern detectors with superior calibration and position correction techniques (Figure 14 bottom and Appendix A).
4. By restricting $L_y(l')$ and $Q_y(l')$ to common WIMP search E_s , NEST errors can be approximated as a flat 15%. As S1 and S2 are proportional to yields, this means that g_1 and g_2 can absorb the errors to first order (*e.g.* $g_1 = 0.15$ instead of 0.17).

Short-term future work includes a NEST re-writing to account for the lower W_q measured by EXO and Baudis et al. [43, 154]. Secondly, there will be a concerted effort to return to a semi-empirical formulation through applying the modified T-I model pioneered by ArgoNeuT [155], combined with a literal breakup of long tracks into boxes as done in the thesis of Dahl, allowing higher energies to exhibit lower light yields without hard-coding, by virtue of being comprised of multiple, lower- E interactions.

Improved modeling of the MeV scale is important for searches for neutrinoless double-beta ($0\nu\beta\beta$) decay, for which the key discrimination is not NR vs. ER, but between two forms of the latter (β vs. γ). EXO-200 [3] and KamLAND-Zen [156] have produced the two most stringent half-life limits for ^{136}Xe , and are highly competitive with Ge-based experiments. In addition to these results, one must evaluate the prospects of nEXO [157], as well as of LZ [158], XENONnT [159], and XLZD [125] in this field of nuclear physics. The dark-matter-focused experiments have higher ER background compared to nEXO, but superior energy resolution.

Longer-term future work on NEST will involve molecular dynamics modeling of individual Xe atoms and ions, starting with the 12-6 Lennard-Jones potential of the van der Waals forces. LXe parameters are known, for L-J and for more advanced models [160]. While these approaches are challenging for MeV energies, at sub-keV scales where yields are more uncertain, fewer interactions are involved, leading to a more computationally tractable problem.

ACKNOWLEDGMENTS

This work was supported by the U.S. Department of Energy under Award DE-SC0015535 and by the National Science Foundation under Awards 2046549 and 2112802. We thank the LZ/LUX, plus XENON1T/nT/DARWIN, collaborations for useful recent discussion as well as continued support for NEST work. We especially thank LUX for providing key detector parameters, and LUX collaborator Prof. Rick Gaitskill (Brown University), Dr. Xin Xiang (formerly of Brown, now at Brookhaven National Laboratory), and Dr. Quentin Riffard (Lawrence Berkeley National Laboratory), for critical discussions regarding the detector performance of a potential Generation-3 liquid Xe TPC detector. We also thank Prof. Liang Yang of UC San Diego/nEXO for his support of Min Zhong.

APPENDIX A: SUMMARY OF NEST MODEL PARAMETERS

In this appendix, we provide tables detailing the functions and model parameters used in NEST for LXe yields from β ER, γ ER, NR, as well as their fluctuations. While NEST has additional models for ^{83m}Kr ER as well as NR from non-Xe nuclei (including α decay), those are not relevant to this work. They can be found in [161].

TABLE III. Table of NEST model parameters comprising the β ER yield models for total light and charge shown in Equation (6).

| | |
|----------|---|
| m_1 | Stitching-region yield for β ER charge yields between low and high energies, depending on field and density: $m_1 = 30.66 + (6.20 - 30.66)/(1 + (\mathcal{E}/73.86)^{2.03})^{0.42}$ at a typical LXe density. Takes values $\mathcal{O}(10 \text{ keV}^{-1})$ for $\mathcal{O}(100 \text{ V/cm})$ fields. |
| m_2 | Low-energy asymptote of the β ER charge yield equation. Default value is approximately 77.3 keV^{-1} . |
| m_3 | Controls the energy-dependent shape of the β charge yields in the low-energy (Thomas-Imel) regime: $m_3 = \log_{10}(\mathcal{E}) \cdot 0.14 + 0.53$. Field-dependent function, with values of approximately 0.8-1.5 keV for $\mathcal{O}(100 \text{ V/cm})$ fields. |
| m_4 | Field-dependent control on the energy-dependent shape of the β charge yields at lower energies: $m_4 = 1.82 + (2.83 - 1.82)/(1 + (\mathcal{E}/144.65)^{-2.81})$. Takes values from approximately 2.0-2.8 for $\mathcal{O}(100 \text{ V/cm})$ fields. |
| m_5 | High-energy asymptote of the β charge yield model. Defined as: $m_5 = \frac{1}{W} \cdot [1 + N_{ex}/N_i]^{-1} - m_1$ (See Ref. [22].) |
| m_6 | Low-energy asymptote of the higher-energy behavior for β ER charge yields. Degenerate with m_1 and explicitly set to 0 keV^{-1} . |
| m_7 | Field-dependent scaling on the behavior of the β charge yields at higher energies: $m_7 = 7.03 + (98.28 - 7.03)/(1 + (\mathcal{E}/256.48)^{1.29})$. Takes values $\mathcal{O}(10 \text{ keV})$ for $\mathcal{O}(100 \text{ V/cm})$ fields. |
| m_8 | Control on the energy-dependent shape of the β charge yields at higher energies. The default value is a constant, 4.3. |
| m_9 | Asymmetry control on the low-energy behavior. The default value is a constant, 0.3. |
| m_{10} | Asymmetry control on the high-energy behavior of the β charge yields model: $m_{10} = 0.05 + (0.12 - 0.05)/(1 + (\mathcal{E}/139.26)^{-0.66})$. Field-dependent function that takes values ~ 0.1 for $\mathcal{O}(100 \text{ V/cm})$ fields. |

TABLE IV. Table of NEST model parameters comprising the γ ER yield models for total light and charge shown in Equation (6). The parameters go into the same functions as those for β ER yields in the previous table.

| | |
|----------|---|
| m_1 | Field-dependent function controlling the transition between lower and higher energies: $m_1 = 34.0 + (3.3 - 34.0)/(1 + (\mathcal{E}/165.3)^{0.7})$. |
| m_2 | Low-energy asymptote of the γ ER charge yield equation, defined as $1/W_q$ in units of keV^{-1} . |
| m_3 | Controls the energy-dependent shape of the γ charge yields in the low-energy (Thomas-Imel) regime; a constant value of 2 keV is used. |
| m_4 | Control on the energy-dependent shape of the γ charge yields at lower energies; a constant power of 2 is used. |
| m_5 | High-energy asymptote of the γ charge yield model. Defined as: $m_5 = 23.2 + (10.7 - 23.1)/(1 + (\mathcal{E}/34.2)^{0.9})$. |
| m_6 | Low-energy asymptote of the higher-energy behavior for γ ER charge yields. Degenerate with m_1 and explicitly set to 0 keV^{-1} . |
| m_7 | Field-dependent and density-dependent scaling on the behavior of the γ charge yields at higher energies: $m_7 = 66.8 + (829.3 - 66.8)/(1 + (\rho^{8.2} \cdot \mathcal{E}/(2.4 \cdot 10^5))^{0.8})$. |
| m_8 | Control on the energy-dependent shape of the γ charge yields at higher energies. Default value is a constant power of 2. |
| m_9 | Asymmetry control on the low-energy behavior: unused for γ ER yields and set to unity. |
| m_{10} | Asymmetry control on the high-energy behavior of the γ charge yields model: unused for γ ER yields and set to unity. |

TABLE V. Table of NEST model parameters comprising the NR mean yield models for total light and charge shown in Equations (13) and (14).

| | |
|-------------|--|
| α | Scaling on NR total quanta. Default value is $11^{+2.0}_{-0.5} \text{ keV}^{-\beta}$. |
| β | Power-law exponent for the NR total quanta. Default value is 1.1 ± 0.05 . |
| ς | Field dependence in NR light and charge yields, with mass-density-dependent scaling (Equation (12)). |
| ρ_0 | Reference density for scaling density-dependent NEST functions: 2.9 g/cm^3 . |
| v | Hypothetical exponential control on density dependence in ς ; the default value is 0.3. |
| δ | Power-law exponent in the field dependence in ς ; default value is -0.0533 ± 0.0068 . |
| γ | Power-law base for the field dependence in ς . Default value is 0.0480 ± 0.0021 . |
| ϵ | Reshaping parameter for NR charge yields, controlling the effective energy scale at which the charge yield behavior changes. The default value is $12.6^{+3.4}_{-2.9} \text{ keV}$. |
| p | Exponent which controls the shape of the energy dependence of the NR charge yields at energies greater than $\mathcal{O}(\epsilon)$. Default value is 0.5. |
| ζ | Controls the energy dependence of the NR charge yields roll-off at low energies. Default value is $0.3 \pm 0.1 \text{ keV}$. |
| η | Controls energy-dependent shape of the NR charge yields roll-off at low energies. Default value is 2 ± 1 . |
| θ | Controls the energy dependence of the NR light yields roll-off. Default value is $0.30 \pm 0.05 \text{ keV}$. |
| ι | Controls the shape of the energy dependence of the NR light yields roll-off. Default value is 2.0 ± 0.5 . |

TABLE VI. Table of NEST model parameters for different types of fluctuations for ERs and NRs.

| | |
|------------|--|
| F_q | Fano-like factor for statistical fluctuations. For ERs, this is proportional to $\sqrt{E \cdot \mathcal{E}}$; see Equation (8). For NRs, this is separated into fluctuations for N_{ex} and N_i ; the default value is 0.4 for both in NEST v2.3.11, while the values were 1.0 in previous NEST versions. |
| σ_p | Non-binomial contribution to recombination fluctuations, modeled as a skew Gaussian in electron fraction space. |
| A | Amplitude of non-binomial recombination skew Gaussian. For NRs, this is a constant 0.04 (v2.3.11) or 0.1 (v2.3.10). For ERs, it is field-dependent: $A = 0.09 + (0.05 - 0.09)/(1 + (\mathcal{E}/295.2)^{251.6})^{0.007}$, where 0.05 was 0.055 in 2.3.10 |
| ξ | Centroid-location parameter of the non-binomial recombination skew Gaussian. Default value for ERs is an electron fraction of 0.45, but 0.5 for NRs. |
| ω | Width parameter for the non-binomial recombination skew Gaussian. Takes value of 0.205 for ERs and 0.19 for NRs. |
| α_p | Skewness parameters for the non-binomial recombination skew Gaussian. Takes the value -0.2 for ERs, while being zero for NRs. |
| α_r | Additional skewness within the recombination process itself. Field- and energy- dependent equations can be found in Ref. [57] for ERs, while it is fixed at 2.25 for NRs, with evidence of higher values in [57] |

- [1] L. Baudis, *European Review* **26**, 70–81 (2018).
- [2] D. S. Akerib *et al.* (LUX Collaboration), *Phys. Rev. D* **103**, 122005 (2021).
- [3] G. Anton *et al.* (EXO-200), *Phys. Rev. Lett.* **123**, 161802 (2019), arXiv:1906.02723 [hep-ex].
- [4] E. Aprile *et al.* (XENON1T Collaboration), *Nature* **568**, 532 (2019), arXiv:1904.11002 [nucl-ex].
- [5] D. S. Akerib *et al.*, *Astroparticle Physics* **125**, 102480 (2021).
- [6] B. Yan *et al.*, *Chinese Physics C* **45**, 075001 (2021).
- [7] E. Aprile *et al.* (XENON Collaboration), *Phys. Rev. Lett.* **126**, 091301 (2021).
- [8] D. Caratelli *et al.*, arXiv only (2022), 10.48550/ARXIV.2203.00740.
- [9] A. A. Abud *et al.* (DUNE Collaboration), *Phys. Rev. D* **107**, 092012 (2023).
- [10] S. Westerdale, “The DEAP-3600 liquid argon optical model and NEST updates,” (In press at JINST), arXiv:2312.07712 [physics.ins-det].
- [11] E. Aprile, R. Budnik, B. Choi, H. A. Contreras, K.-L. Giboni, L. W. Goetzke, J. E. Koglin, R. F. Lang, K. E. Lim, A. J. Melgarejo Fernandez, R. Persiani, G. Plante, and A. Rizzo, *Phys. Rev. D* **86**, 112004 (2012).
- [12] L. Baudis, H. Dujmovic, C. Geis, A. James, A. Kish, A. Manalaysay, T. Marrodan Undagoitia, and M. Schumann, *Phys. Rev. D* **87**, 115015 (2013), arXiv:1303.6891 [astro-ph.IM].
- [13] T. Doke, A. Hitachi, J. Kikuchi, K. Masuda, H. Okada, and E. Shibamura, *Japanese Journal of Applied Physics* **41**, 1538 (2002).
- [14] E. Aprile *et al.* (XENON), *Phys. Rev. D* **99**, 112009 (2019), arXiv:1902.11297 [physics.ins-det].
- [15] C. E. Dahl, *The physics of background discrimination in liquid xenon, and first results from XENON10 in the hunt for WIMP dark matter*, Ph.D. thesis, Princeton University (2009).
- [16] E. M. Boulton *et al.*, *JINST* **12**, P08004 (2017), arXiv:1705.08958 [physics.ins-det].
- [17] D. Akerib *et al.* (LUX), *Phys. Rev. D* **100**, 022002 (2019), arXiv:1903.12372 [physics.ins-det].
- [18] E. Aprile *et al.* (XENON Collaboration), *Phys. Rev. D* **97**, 092007 (2018).
- [19] D. S. Akerib *et al.*, *Phys. Rev. D* **96**, 112011 (2017).
- [20] L. Goetzke, E. Aprile, M. Anthony, G. Plante, and M. Weber, *Phys. Rev. D* **96**, 103007 (2017), arXiv:1611.10322 [astro-ph.IM].
- [21] D. Akimov *et al.*, *Journal of Instrumentation* **9**, P11014 (2014).
- [22] D. S. Akerib *et al.*, *Journal of Instrumentation* **15**, T02007 (2020).
- [23] M. Szydagis, G. A. Block, C. Farquhar, A. J. Flesher, E. S. Kozlova, C. Levy, E. A. Mangus, M. Mooney, J. Mueller, G. R. C. Rischbieter, and A. K. Schwartz, *Instruments* **5**, 13 (2021).
- [24] M. Szydagis *et al.*, “NEST: Noble Element Simulation Technique, A Symphony of Scintillation <http://nest.physics.ucdavis.edu>,” (2020).
- [25] E. Conti, R. DeVoe, G. Gratta, T. Koffas, S. Waldman, J. Wodin, D. Akimov, G. Bower, M. Breidenbach, R. Conley, M. Danilov, Z. Djurcic, A. Dolgolenko, C. Hall, A. Odian, A. Piepke, C. Y. Prescott, P. C. Rowson, K. Skarpaas, J.-L. Vuilleumier, K. Wamba, and O. Zeldovich, *Phys. Rev. B* **68**, 054201 (2003).
- [26] G. Bressi, G. Carugno, E. Conti, C. Noce, and D. Iannuzzi, *Nuclear Instruments and Methods in Physics Research Section A: Accelerators, Spectrometers, Detectors and Associated Equipment* **461**, 378 (2001), 8th Pisa Meeting on Advanced Detectors.
- [27] E. Aprile, A. E. Bolotnikov, A. I. Bolozdynya, and T. Doke, “Noble Fluids as Detector Media,” in *Noble Gas Detectors* (John Wiley & Sons, Ltd, 2006) pp. 16–17.
- [28] M. Szydagis, C. Levy, G. Blockinger, A. Kamaha, N. Parveen, and G. Rischbieter, *Phys. Rev. D* **103**, 012002 (2021), arXiv:2007.00528 [hep-ex].
- [29] T. Doke, A. Hitachi, J. Kikuchi, K. Masuda, H. Okada, and E. Shibamura, *Japanese Journal of Applied Physics* **41**, 1538 (2002).
- [30] D. S. Akerib *et al.*, *Phys. Rev. D* **93**, 072009 (2016).
- [31] Q. Lin, J. Fei, F. Gao, J. Hu, Y. Wei, X. Xiao, H. Wang, and K. Ni, *Phys. Rev. D* **92**, 032005 (2015), arXiv:1505.00517 [physics.ins-det].
- [32] I. Obodovskii and K. Ospanov, *Instruments and Experimental Techniques* **37**, 42 (1994).
- [33] M. Yamashita, T. Doke, K. Kawasaki, J. Kikuchi, and S. Suzuki, *Nuclear Instruments and Methods in Physics Research Section A: Accelerators, Spectrometers, Detectors and Associated Equipment* **535**, 692 (2004).
- [34] D. S. Akerib *et al.* (LUX Collaboration), *Phys. Rev. D* **95**, 012008 (2017).
- [35] A. Tan *et al.* (PandaX-II Collaboration), *Phys. Rev. Lett.* **117**, 121303 (2016).
- [36] E. Aprile *et al.* (XENON100 Collaboration), *Phys. Rev. Lett.* **105**, 131302 (2010).
- [37] E. Aprile *et al.*, *Astroparticle Physics* **34**, 679 (2011).
- [38] J. Thomas and D. A. Imel, *Phys. Rev. A* **36**, 614 (1987).
- [39] T. Doke, H. J. Crawford, A. Hitachi, J. Kikuchi, P. J. Lindstrom, K. Masuda, E. Shibamura, and T. Takahashi, *Nuclear Instruments and Methods in Physics Research Section A: Accelerators, Spectrometers, Detectors and Associated Equipment* **269**, 291 (1988).
- [40] M. Szydagis *et al.*, “Noble element simulation technique <https://doi.org/10.5281/zenodo.6989015>,” (2022).
- [41] M. Szydagis, N. Barry, K. Kazkaz, J. Mock, D. Stolp, M. Sweany, M. Tripathi, S. Uvarov, N. Walsh, and M. Woods, *JINST* **6**, P10002 (2011), arXiv:1106.1613 [physics.ins-det].
- [42] M. Berger, J. Coursey, M. Zucker, and J. Chang, “ESTAR, PSTAR, and ASTAR: Computer Programs for Calculating Stopping-Power and Range Tables for Electrons, Protons, and Helium Ions,” (National Institute of Standards and Technology, Gaithersburg, MD 2005).
- [43] G. Anton *et al.* (EXO-200), *Phys. Rev. C* **101**, 065501 (2020), arXiv:1908.04128 [physics.ins-det].
- [44] M. Szydagis, A. Fyhrie, D. Thorngren, and M. Tripathi, *JINST* **8**, C10003 (2013), arXiv:1307.6601 [physics.ins-det].
- [45] T. Doke, A. Hitachi, S. Kubota, A. Nakamoto, and T. Takahashi, *Nuclear Instruments and Methods* **134**, 353 (1976).
- [46] V. Alvarez *et al.* (NEXT), *Nucl. Instrum. Meth. A* **708**, 101 (2013), arXiv:1211.4474 [physics.ins-det].

- [47] S. Delaquis *et al.*, *Journal of Instrumentation* **13**, P08023 (2018).
- [48] E. Aprile *et al.*, *The European Physical Journal C* **80**, 8 (2020).
- [49] E. Aprile, K. L. Giboni, P. Majewski, K. Ni, and M. Yamashita, *Phys. Rev. B* **76**, 014115 (2007).
- [50] E. Aprile, R. Mukherjee, and M. Suzuki, *Nuclear Instruments and Methods in Physics Research Section A: Accelerators, Spectrometers, Detectors and Associated Equipment* **302**, 177 (1991).
- [51] R. L. Platzman, *International Journal of Applied Radiation and Isotopes* **10**, 116 (1961).
- [52] A. Dobi, *Measurement of the Electron Recoil Band of the LUX Dark Matter Detector With a Tritium Calibration Source*, Ph.D. thesis, Maryland U., College Park (2014).
- [53] S. Amoroso *et al.*, *Nuclear Instruments and Methods in Physics Research Section A: Accelerators, Spectrometers, Detectors and Associated Equipment* **523**, 275 (2004).
- [54] J. Thomas, D. A. Imel, and S. Biller, *Phys. Rev. A* **38**, 5793 (1988).
- [55] D. R. Nygren, *Journal of Physics: Conference Series* **460**, 012006 (2013).
- [56] C. Davis *et al.* (EXO-200), *JINST* **11**, P07015 (2016), arXiv:1605.06552 [physics.ins-det].
- [57] D. S. Akerib *et al.* (LUX Collaboration), *Phys. Rev. D* **102**, 112002 (2020).
- [58] G. R. C. Rischbieter, *Signal Yields and Detector Modeling in Xenon Time Projection Chambers, and Results of an Effective Field Theory Dark Matter Search Using LUX Data*, Ph.D. thesis, UAlbany SUNY (2022).
- [59] V. Y. Chepel *et al.*, *Proceedings of the 1999 IEEE 13th International Conference on Dielectric Liquids*, 52 (1999).
- [60] F. Arneodo *et al.*, *Nucl. Inst. and Meth. A* **449**, 147 (2000).
- [61] D. Akimov *et al.*, *Phys. Lett. B* **524**, 245 (2002).
- [62] E. Aprile *et al.*, *Phys. Rev. D* **72**, 072006 (2005).
- [63] E. Aprile, L. Baudis, B. Choi, K. L. Giboni, K. Lim, A. Manalaysay, M. E. Monzani, G. Plante, R. Santorelli, and M. Yamashita, *Phys. Rev. C* **79**, 045807 (2009).
- [64] A. Manzur, A. Curioni, L. Kastens, D. McKinsey, K. Ni, and T. Wongjirad, *Phys. Rev. C* **81**, 025808 (2010), arXiv:0909.1063 [physics.ins-det].
- [65] G. Plante *et al.*, *Phys. Rev. C* **84**, 045805 (2011).
- [66] E. Aprile *et al.* (XENON), *Phys. Rev. Lett.* **119**, 181301 (2017), arXiv:1705.06655 [astro-ph.CO].
- [67] D. S. Akerib *et al.*, arXiv only (2016), arXiv:1608.05381 [physics.ins-det].
- [68] D. S. Akerib *et al.* (LUX Collaboration), *Phys. Rev. Lett.* **118**, 021303 (2017).
- [69] D. Huang, *Ultra-Low Energy Calibration of the LUX and LZ Dark Matter Detectors*, Ph.D. thesis, Brown U. (2020).
- [70] D. S. Akerib *et al.*, “Improved Dark Matter Search Sensitivity Resulting from LUX Low-Energy Nuclear Recoil Calibration (submitted to PRL),” (2022).
- [71] E. Aprile, M. Anthony, Q. Lin, Z. Greene, P. de Perio, F. Gao, J. Howlett, G. Plante, Y. Zhang, and T. Zhu, *Phys. Rev. D* **98**, 112003 (2018).
- [72] B. Lenardo, J. Xu, S. Pereverzev, O. A. Akindele, D. Naim, J. Kingston, A. Bernstein, K. Kazkaz, M. Tripathi, C. Awe, L. Li, J. Runge, S. Hedges, P. An, and P. S. Barbeau, “Measurement of the ionization yield from nuclear recoils in liquid xenon between 0.3 – 6 keV with single-ionization-electron sensitivity,” (2019), arXiv:1908.00518 [physics.ins-det].
- [73] M. Horn *et al.*, *Physics Letters B* **705**, 471–476 (2011).
- [74] P. Sorensen *et al.*, *PoS IDM2010*, 017 (2011), arXiv:1011.6439 [astro-ph.IM].
- [75] P. Sorensen and C. E. Dahl, *Phys. Rev. D* **83**, 063501 (2011).
- [76] C. Faham, V. Gehman, A. Currie, A. Dobi, P. Sorensen, and R. Gaitskell, *Journal of Instrumentation* **10**, P09010 (2015).
- [77] B. Edwards *et al.*, *JINST* **13**, P01005 (2018), arXiv:1710.11032 [physics.ins-det].
- [78] J. Xu, S. Pereverzev, B. Lenardo, J. Kingston, D. Naim, A. Bernstein, K. Kazkaz, and M. Tripathi, *Phys. Rev. D* **99**, 103024 (2019), arXiv:1904.02885 [physics.ins-det].
- [79] J. Aalbers *et al.*, “First Constraints on WIMP-Nucleon Effective Field Theory Couplings in an Extended Energy Region From LUX-ZEPLIN,” (2023), arXiv:2312.02030 [hep-ex].
- [80] J. Lindhard, *Mat. Fys. Medd. K. Dan. Vidensk. Selsk.* **33**, 10 (1963).
- [81] P. Sorensen, *Phys. Rev. D* **91**, 083509 (2015).
- [82] E. Aprile *et al.* (XENON Collaboration), *Phys. Rev. Lett.* **123**, 241803 (2019).
- [83] A. Hitachi, *Astroparticle Physics* **24**, 247 (2005).
- [84] E. Aprile, C. E. Dahl, L. de Viveiros, R. J. Gaitskell, K. L. Giboni, J. Kwong, P. Majewski, K. Ni, T. Shutt, and M. Yamashita, *Phys. Rev. Lett.* **97**, 081302 (2006).
- [85] U. Fano, *Phys. Rev.* **72**, 26 (1947).
- [86] G. Plante, *The XENON100 Dark Matter Experiment: Design, Construction, Calibration and 2010 Search Results with Improved Measurement of the Scintillation Response of Liquid Xenon to Low-Energy Nuclear Recoils*, Ph.D. thesis, Columbia U. (main) (2012).
- [87] D. S. Akerib *et al.* (LUX Collaboration), *Phys. Rev. Lett.* **122**, 131301 (2019).
- [88] L. Wang and D. M. Mei, *J. Phys. G* **44**, 055001 (2017), arXiv:1604.01083 [physics.ins-det].
- [89] D. S. Akerib *et al.* (LUX), *Phys. Rev. Lett.* **112**, 091303 (2014), arXiv:1310.8214 [astro-ph.CO].
- [90] E. Aprile *et al.* (XENON Collaboration), *Phys. Rev. D* **102**, 072004 (2020).
- [91] J. Birks, *The Theory and Practice of Scintillation Counting*, International Series of Monographs in Electronics and Instrumentation (Pergamon, 1964).
- [92] D.-M. Mei, Z.-B. Yin, L. Stonehill, and A. Hime, *Astroparticle Physics* **30**, 12–17 (2008).
- [93] P. Sorensen *et al.*, *Nuclear Instruments and Methods in Physics Research Section A: Accelerators, Spectrometers, Detectors and Associated Equipment* **601**, 339–346 (2009).
- [94] W. Mu, X. Xiong, and X. Ji, *Astroparticle Physics* **61**, 56 (2015).
- [95] F. Bezrukov, F. Kahlhoefer, and M. Lindner, *Astroparticle Physics* **35**, 119–127 (2011).
- [96] W. Mu and X. Ji, *Astroparticle Physics* **62**, 108 (2015).
- [97] Y. Sarkis, A. Aguilar-Arevalo, and J. C. D’Olivo, *Phys. Rev. D* **101**, 102001 (2020).
- [98] B. Lenardo, K. Kazkaz, A. Manalaysay, J. Mock, M. Szydagis, and M. Tripathi, *IEEE Trans. Nucl. Sci.* **62**, 3387 (2015), arXiv:1412.4417 [astro-ph.IM].
- [99] P. Sorensen, *Nuclear Instruments and Methods in Physics Research Section A: Accelerators, Spectrom-*

- eters, Detectors and Associated Equipment **635**, 41 (2011).
- [100] D. S. Akerib *et al.* (LUX), Phys. Rev. Lett. **116**, 161301 (2016), arXiv:1512.03506 [astro-ph.CO].
- [101] A. Mozumder, Chemical Physics Letters **238**, 143 (1995).
- [102] J. Albert *et al.* (EXO-200), Phys. Rev. C **95**, 025502 (2017), arXiv:1609.04467 [physics.ins-det].
- [103] R. James, J. Palmer, A. Kaboth, C. Ghag, and J. Aalbers, Journal of Instrumentation **17**, P08012 (2022).
- [104] D. S. Akerib *et al.*, Astroparticle Physics **62**, 33 (2015).
- [105] J. Verbus *et al.*, Nucl. Instrum. Meth. A **851**, 68 (2017), arXiv:1608.05309 [physics.ins-det].
- [106] J. Angle *et al.* (XENON), Phys. Rev. Lett. **100**, 021303 (2008), arXiv:0706.0039 [astro-ph].
- [107] M. Szydagis *et al.* (LUX), in *10th International Symposium on Cosmology and Particle Astrophysics* (2014) arXiv:1402.3731 [hep-ex].
- [108] J. Mock, N. Barry, K. Kazkaz, M. Szydagis, M. Tripathi, S. Uvarov, M. Woods, and N. Walsh, JINST **9**, T04002 (2014), arXiv:1310.1117 [physics.ins-det].
- [109] D. S. Akerib *et al.* (LUX), Phys. Rev. **D97**, 102008 (2018), arXiv:1712.05696 [physics.ins-det].
- [110] D. S. Akerib *et al.*, Nucl. Instrum. Meth. **A675**, 63 (2012), arXiv:1111.2074 [physics.data-an].
- [111] D. S. Akerib *et al.* (LUX), Phys. Rev. **D97**, 112002 (2018), arXiv:1802.06162 [physics.ins-det].
- [112] D. S. Akerib *et al.* (LUX Collaboration), Phys. Rev. D **101**, 042001 (2020).
- [113] J. R. Verbus, *An Absolute Calibration of Sub-1 keV Nuclear Recoils in Liquid Xenon Using D-D Neutron Scattering Kinematics in the LUX Detector*, Ph.D. thesis, Brown U. (2016).
- [114] D. S. Akerib *et al.* (LUX Collaboration), Phys. Rev. D **106**, 072009 (2022).
- [115] D. Akerib *et al.* (LUX Collaboration), Phys. Rev. D **96**, 112009 (2017), arXiv:1708.02566 [physics.ins-det].
- [116] S. Agostinelli *et al.*, Nuclear Instruments and Methods in Physics Research Section A: Accelerators, Spectrometers, Detectors and Associated Equipment **506**, 250 (2003).
- [117] J. Allison *et al.*, IEEE Trans. Nucl. Sci. **53**, 270 (2006).
- [118] H. Araújo, “Revised performance parameters of the ZEPLIN-III dark matter experiment,” (2020), arXiv:2007.01683 [physics.ins-det].
- [119] N. Priel, L. Rauch, H. Landsman, A. Manfredini, and R. Budnik, Journal of Cosmology and Astroparticle Physics **2017**, 013 (2017).
- [120] A. L. Fitzpatrick, W. Haxton, E. Katz, N. Lubbers, and Y. Xu, JCAP **1302**, 004 (2013), arXiv:1203.3542 [hep-ph].
- [121] K. Arisaka, P. Beltrame, C. Ghag, K. Lung, and P. Scovell, Astroparticle Physics **37**, 51 (2012).
- [122] D. S. Akerib *et al.* (LUX Collaboration), Phys. Rev. D **104**, 062005 (2021).
- [123] V. N. Lebedenko *et al.*, Phys. Rev. **D80**, 052010 (2009), arXiv:0812.1150 [astro-ph].
- [124] R. F. Lang, A. Brown, E. Brown, M. Cervantes, S. Macmullin, D. Masson, J. Schreiner, and H. Simgen, JINST **11**, P04004 (2016), arXiv:1602.01138 [physics.ins-det].
- [125] J. Aalbers *et al.*, Journal of Physics G: Nuclear and Particle Physics **50**, 013001 (2022).
- [126] E. Aprile *et al.* (XENON Collaboration), Phys. Rev. Lett. **123**, 251801 (2019).
- [127] D. S. Akerib *et al.* (LUX-ZEPLIN Collaboration), Phys. Rev. D **101**, 052002 (2020).
- [128] B. J. Mount *et al.* (LZ Collaboration), arXiv only (2017), arXiv:1703.09144.
- [129] D. S. Akerib *et al.* (LUX Collaboration), Nucl.Instrum.Meth. **A668**, 1 (2012), arXiv:1108.1836 [astro-ph.IM].
- [130] D. S. Akerib *et al.* (LUX Collaboration), Nucl.Instrum.Meth. **A818**, 57 (2016), arXiv:1511.03541 [physics.ins-det].
- [131] P. Sorensen, *A Position-Sensitive Liquid Xenon Time-Projection Chamber for Direct Detection of Dark Matter: The XENON10 Experiment*, Ph.D. thesis, Brown University (2008).
- [132] L. de Viveiros, *Optimization of Signal versus Background in Liquid Xe Detectors Used for Dark Matter Direct Detection Experiments*, Ph.D. thesis, Brown University (2010).
- [133] J. Aalbers *et al.*, “First Dark Matter Search Results from the LUX-ZEPLIN (LZ) Experiment (accepted by PRL),” (2022).
- [134] T. Pershing, D. Naim, B. G. Lenardo, J. Xu, J. Kingston, E. Mizrachi, V. Mozin, P. Kerr, S. Pereverzev, A. Bernstein, and M. Tripathi, Phys. Rev. D **106**, 052013 (2022).
- [135] W. H. Lippincott, K. J. Coakley, D. Gastler, A. Hime, E. Kearns, D. N. McKinsey, J. A. Nikkel, and L. C. Stonehill, Phys. Rev. C **78**, 035801 (2008).
- [136] C. Amole *et al.* (PICO Collaboration), Phys. Rev. Lett. **118**, 251301 (2017).
- [137] E. Aprile *et al.* (XENON Collaboration), Phys. Rev. Lett. **129**, 161805 (2022).
- [138] G. R. C. Rischbieter, meetings.aps.org/ Meeting/APR20/Session/R13.2 (April 2020 APS Meeting).
- [139] E. Aprile *et al.* (XENON), Phys. Rev. D **100**, 052014 (2019), arXiv:1906.04717 [physics.ins-det].
- [140] M. Xiao *et al.* (PandaX), Sci. China Phys. Mech. Astron. **57**, 2024 (2014), arXiv:1408.5114 [hep-ex].
- [141] E. Aprile *et al.*, “First Dark Matter Search with Nuclear Recoils from the XENONnT Experiment,” (2023), arXiv:2303.14729 [hep-ex].
- [142] K. Ueshima *et al.*, Nuclear Instruments and Methods in Physics Research Section A: Accelerators, Spectrometers, Detectors and Associated Equipment **659**, 161 (2011).
- [143] D. S. Akerib *et al.*, ArXiv e-prints (2015), arXiv:1509.02910 [physics.ins-det].
- [144] J. Aalbers *et al.* (DARWIN), JCAP **11**, 017 (2016), arXiv:1606.07001 [astro-ph.IM].
- [145] F. Kuger, “Charge signal measurement by scintillation in liquid xenon,” (ECFA TF2 Symposium, April 09 2021).
- [146] D. S. Akerib *et al.*, Phys. Rev. D **102**, 092004 (2020).
- [147] J. Kwong, P. Brusov, T. Shutt, C. Dahl, A. Bolozdynya, and A. Bradley, Nuclear Instruments and Methods in Physics Research Section A: Accelerators, Spectrometers, Detectors and Associated Equipment **612**, 328 (2010).
- [148] K. Abe *et al.* (XMASS Collaboration), Phys. Rev. Lett. **113**, 121301 (2014).
- [149] E. Hogenbirk, M. Decowski, K. McEwan, and A. Colijn, JINST **13**, P10031 (2018), arXiv:1807.07121 [physics.ins-det].

- [150] S. Kubota, A. Nakamoto, T. Takahashi, T. Hamada, E. Shibamura, M. Miyajima, K. Masuda, and T. Doke, *Phys. Rev. B* **17**, 2762 (1978).
- [151] J. Dawson, A. Howard, D. Akimov, H. Araújo, A. Bewick, D. Davidge, W. Jones, M. Joshi, V. Lebedenko, I. Liubarsky, J. Quenby, G. Rochester, D. Shaul, T. Sumner, and R. Walker, *Nuclear Instruments and Methods in Physics Research Section A: Accelerators, Spectrometers, Detectors and Associated Equipment* **545**, 690 (2005).
- [152] B. Adams, A. Elagin, H. Frisch, R. Obaid, E. Oberla, A. Vostrikov, R. Wagner, J. Wang, and M. Wetstein, *Nuclear Instruments and Methods in Physics Research Section A: Accelerators, Spectrometers, Detectors and Associated Equipment* **795**, 1 (2015).
- [153] T. Tsang, A. Bolotnikov, A. Haarahiltunen, and J. Heinonen, *Opt. Express* **28**, 13299 (2020).
- [154] L. Baudis, P. Sanchez-Lucas, and K. Thieme, *The European Physical Journal C* **81**, 1060 (2021).
- [155] R. Acciarri *et al.*, *Journal of Instrumentation* **8**, P08005 (2013).
- [156] S. Abe *et al.* (KamLAND-Zen Collaboration), *Phys. Rev. Lett.* **130**, 051801 (2023).
- [157] J. B. Albert *et al.* (nEXO Collaboration), *Phys. Rev. C* **97**, 065503 (2018).
- [158] D. S. Akerib *et al.* (LUX-ZEPLIN (LZ) Collaboration), *Phys. Rev. C* **102**, 014602 (2020).
- [159] E. Aprile *et al.* (XENON Collaboration), *Phys. Rev. C* **106**, 024328 (2022).
- [160] G. Rutkai, M. Thol, R. Span, and J. Vrabec, *Molecular Physics* **115**, 1104 (2017), <https://doi.org/10.1080/00268976.2016.1246760>.
- [161] M. Szydakis *et al.*, “Noble Element Simulation Technique <https://doi.org/10.5281/zenodo.7061832>,” (2022).